

2017

Surface acoustic wave sensor for low concentration mercury vapor detection

<https://hdl.handle.net/2144/20833>

"Downloaded from OpenBU. Boston University's institutional repository."

BOSTON UNIVERSITY
COLLEGE OF ENGINEERING

Thesis

**SURFACE ACOUSTIC WAVE SENSOR FOR LOW CONCENTRATION
MERCURY VAPOR DETECTION**

by

YISHEN LU

B.E., China University of Mining and Technology, 2015

Submitted in partial fulfillment of the
requirements for the degree of
Master of Science

2017

© 2017 by
YISHEN LU
All rights reserved

Approved by

First Reader

Xin Zhang, Ph.D.
Professor of Mechanical Engineering
Professor of Materials Science and Engineering

Second Reader

Katherine Yanhang Zhang, Ph.D.
Associate Professor of Mechanical Engineering
Associate Professor of Materials Science and Engineering

Third Reader

Chuanhua Duan, Ph.D.
Assistant Professor Mechanical Engineering
Assistant Professor Materials Science and Engineering

ACKNOWLEDGMENTS

First of all, I would like to thank my advisor, Professor Zhang for giving me the great opportunity to do research in Laboratory of Microsystem Technology. I appreciate the guidance she gave me in this year. It is a meaningful and memorable experience, which helped me develop scientific thinking and technical skills in research and practical areas. I also want to thank Professor Katherine Zhang and Professor Duan for their time to be my committee, insightful comments and advice.

Next, I would like to thank the group members in Laboratory of Microsystem Technology for their support and help in this year. Special thanks to Aobo, for being a good teacher and friend. He helped me in every aspect from the beginning of my research, and I learned a lot from him both in experimental skills and research skills. Xiaoguang and Guangwu are always warm-hearted and willing to answer my questions. Their knowledge and experience are one of the most valuable resources I had during my research. Reza kindly gave me many advices on the direction of the mercury sensing project. And I would like to thank Zhikuan and Xuefei who generously shared research experience and suggestions with me.

Finally, I would like to thank my parents for all of their love, patient, and encouragement in all situations. And thank all my friends for their support.

Additionally, I would like to thank Boston University and Photonic Center for offering me the chance to do all of these.

**SURFACE ACOUSTIC WAVE SENSOR FOR LOW CONCENTRATION
MERCURY VAPOR DETECTION**

YISHEN LU

Boston University, College of Engineering, 2017

Major Professor: Xin Zhang, Ph.D., Professor of Mechanical Engineering, Professor of Materials Science and Engineering

ABSTRACT

Mercury (Hg) has always been a serious risk to the environment and human health. It is a very common contamination in petroleum industry, which may lower product quality, threaten operation safety and worker's health even at a very low concentration. Consequently the detection of mercury is very necessary. Gold is widely used as sensing material of mercury because it has a specific affinity with mercury and the adsorption of mercury changes characteristics of gold such as resistivity and effective mass density. In this thesis, common methods for sensing mercury vapor concentration were summarized and a surface acoustic wave (SAW) sensor utilizing the adsorption of mercury on gold electrodes was proposed for $1 \mu\text{g}/\text{m}^3$ level low concentration mercury vapor detection.

The working principle of SAW sensor was studied and finite element method models were built to optimize the sensor design. The influence of several physical structure parameters such as electrode width and pitch on the sensor sensitivity and response time were studied using the simulation model. According to the simulation

results a prototype of SAW sensor was designed and fabricated. The sensor was then analyzed with network analyzer and tested with mercury vapor. Preliminary results were presented and analyzed in this work. Finally potential future work was proposed and discussed.

TABLE OF CONTENTS

ACKNOWLEDGMENTS.....	iv
ABSTRACT.....	vi
TABLE OF CONTENTS.....	viii
LIST OF TABLES.....	xi
LIST OF FIGURES.....	xii
CHAPTER ONE: INTRODUCTION.....	1
1.1 Motivation of This Work.....	2
1.1.1 Negative effect of mercury in industries.....	2
1.1.2 The health impact of mercury.....	5
1.2 Commonly Used Methods For Mercury Vapor Detection.....	7
1.2.1 Cold vapor atomic absorption spectroscopy (CVAAS).....	7
1.2.2 Cold vapor atomic fluorescence spectrometry (CVAFS).....	8
1.2.3 Microcantilever sensor.....	9
1.2.4 Surface plasmon resonance sensor.....	11
1.2.5 Resistivity (conductivity) sensor.....	12
1.2.6 Surface acoustic wave(SAW) sensor.....	13
1.3 Previous Work.....	16

CHAPTER TWO: THEORETICAL MODEL OF SENSING MERCURY VAPOR

WITH SURFACE ACOUSTIC WAVE (SAW) SENSOR..... 25

2.1 Surface Acoustic (Rayleigh) Wave.....25

2.2 The Piezoelectric Effect..... 26

2.3 Adsorption of Mercury on Gold..... 27

2.4 SAW Velocity (Frequency) Perturbation Theory..... 29

CHAPTER THREE: FEM SIMULATION AND DESIGN OF THE SAW SENSOR

..... 32

3.1 FEM Simulation Model Parameters And Boundary Conditions..... 32

3.2 Optimizing The SAW Sensor Design Through FEM Simulation..... 37

3.2.1 Resonance frequency and sensor characterization..... 37

3.2.2 Effect of electrode width and pitch..... 44

3.2.3 Effect of delay line lengths..... 53

3.3 Summary of FEM Simulation And Design of SAW Sensor.....55

CHAPTER FOUR: DEVICE FABRICATION AND TEST.....56

4.1 SAW Sensor Fabrication..... 56

4.1.1 General steps of SAW sensor fabrication..... 56

4.1.2 Cleaning and photoresist coating..... 57

4.1.3 Exposure and development..... 57

4.1.4 Metal deposition and lift-off.....	63
4.1.5 Dicing saw cutting and printed circuit board (PCB) bonding.....	64
4.1.6 Fabrication summary.....	67
4.2 SAW Sensor Test And Mercury Sensing Experiment.....	68
4.2.1 Test setup.....	68
4.2.2 Resonance frequency test.....	72
4.2.3 Mercury vapor test.....	75
CHAPTER FIVE: RESULTS AND DISCUSSION.....	77
5.1 Frequency Response Analyze.....	77
5.2 Sensor Response To Mercury Vapor Exposure.....	80
5.3 Summary.....	82
CHAPTER SIX: CONCLUSION AND FUTURE WORK.....	85
6.1 Conclusion.....	85
6.2 Potential Improvement And Future Work.....	85
REFERENCES.....	88
CURRICULUM VITAE.....	93

LIST OF TABLES

Table 1. Model parameters in simulation.....	33
Table 2. Characteristics of ST-cut quartz and Y cut quartz.....	35
Table 3. Design parameters of SAW sensor.....	55
Table 4. Frequency data from mercury exposure experiment.....	82

LIST OF FIGURES

Figure 1	Schematic of LME.....	3
Figure 2	Schematic of amalgamation corrosion.....	4
Figure 3	Schematic of CVAAS.....	7
Figure 4	Schematic of CVAFS.....	9
Figure 5	Microcantilever array.....	9
Figure 6	Schematic of deflection microcantilever sensor.....	10
Figure 7	(a) Absorption figure of gold nanoparticle film on quartz. (b) The trace of peak shift during exposure to mercury vapor.....	12
Figure 8	A resistivity based mercury sensor design.....	13
Figure 9	Schematic of a typical SAW sensor structure	14
Figure 10	Schematic of SAW sensor with gold IDTs as sensing element.....	15
Figure 11	Resistivity sensor version 1.....	16
Figure 12	Result of sensor version 1 test (a) reference resistor measurement (b) testing resistor measurement.....	17
Figure 13	SEM results (a) gold surface before exposure (b) gold surface after 10 hours exposure.....	18
Figure 14	Sensor version 2 with temperature sensor.....	19
Figure 15	(a) Resistance measurement result of 3 days 40 ng/m ³ exposure (b) Resistance	

measurement result of 4 days 40 ng/m ³ exposure (c) Resistance difference of 3 days 40 ng/m ³ exposure (d) Resistance difference of 4 days 40 ng/m ³ exposure.....	19
Figure 16 (a) Resistance measurement under mercury vapor concentration 40ng/m ³ , 2L/min with sensor version 2 (b) Resistance difference under 40ng/m ³ , 2L/min (c) Resistance measurement under 20ng/m ³ ,4L/min with sensor version 2 (d) Resistance difference under 20ng/m ³ ,4L/min	20
Figure 17 Comparison between resistive sensor (left) and Wheatstone bridge(right).....	21
Figure 18 Wheatstone bridge sensor with temperature reference.....	22
Figure 19 Normalized test result of selective filter coated sensor (a) sensor output, blue curve is mercury sensor output, red curve is temperature reference. (b) Difference of two output.....	23
Figure 20 (a) Bulk longitudinal (compressional) wave (b) Bulk transverse (shear) wave (c) Surface acoustic (Rayleigh) wave (d) Waves in solid plates	25
Figure 21 (a) Image of gold substrate exposed to 30 ng/L mercury vapor at room temperature (right) and 60°C (right) for 360 minutes (b)The adsorption mechanism of mercury on gold.....	28
Figure 22 Schematic of the SAW sensor model. All electrodes are gold and substrate is ST-cut quartz.....	34
Figure 23 Orientation of ST-cut quartz	35
Figure 24 (a) Custom mesh built in FEM model (b) Mesh near an electrode. Areas closer	

to the electrode got finer mesh elements.....	36
Figure 25 Simulation result of resonant frequencies for sensor with (a) 24 μm pitch, 6 μm electrode width (b) 20 μm pitch, 5 μm electrode width.....	38
Figure 26 The displacement field of sensor with (a) 24 μm pitch, 6 μm electrode width at 138.6MHz, (b) 20 μm pitch, 5 μm electrode width at 169MHz, (c) 20 μm pitch, 5 μm electrode width at 163 MHz.....	40
Figure 27 Simulated negative frequency shift due to mercury absorption.....	43
Figure 28 Relationship between number of monolayers and magnitude of frequency shift, sensor with 24 μm pitch, 6 μm electrode width.....	43
Figure 29 Frequency shift of sensor with 24 μm pitch (A) 5 μm electrode width (B) 6 μm electrode width (C) 7 μm electrode width (D) 8 μm electrode width.....	45
Figure 30 Frequency shift of sensor with 20 μm pitch (A) 5 μm electrode width (B) 6 μm electrode width (C) 7 μm electrode width.....	46
Figure 31 Comparison between sensors with same electrode width but different pitch...47	47
Figure 32 Simulated response time for sensors with 24 μm pitch (A) 5 μm electrode width (B) 6 μm electrode width (C) 7 μm electrode width (D) 8 μm electrode width.....	50
Figure 33 Simulated response time for sensors with 20 μm pitch (A) 5 μm electrode width (B) 6 μm electrode width (C) 7 μm electrode width.....	51
Figure 34 Comparison of the response of sensor with 24 μm pitch, 7 μm electrode	

width and 20 μm pitch, 6 μm electrode width (a) sensitivity, (b) response time.....	52
Figure 35 Simulated sensitivity of sensor with 20 μm pitch 6 μm electrode width with different delay line length.....	54
Figure 36 The fabrication process of the sensor.....	56
Figure 37 A schematic of lift-off process with positive and negative photoresists.....	58
Figure 38 Microscope figure of IDT patterns on silicon wafer with 3 s exposure time and 1 min hard bake.....	61
Figure 39 Microscope figure of IDT patterns on ST-cut quartz wafer with 3 s exposure time and 1 min hard bake.....	62
Figure 40 Microscope figure of IDT patterns on ST-cut quartz wafer with 3 s exposure time and 1.5 min hard bake.....	62
Figure 41 Sample during lift-off process.....	63
Figure 42 Fabricated SAW sensor.....	64
Figure 43 Laser printing machine.....	65
Figure 44 PCB after laser printing.....	66
Figure 45 PCB with welded SMA connector.....	66
Figure 46 Sample SAW sensor.....	67
Figure 47 The computer control unit of the test setup.....	69
Figure 48 PSA 10.536L Hg generator.....	70

Figure 49 Schematic Diagram of Hg generating system.....	70
Figure 50 Structure of the test chamber.....	71
Figure 51 The schematic of test setup airflow.....	72
Figure 52 Measured frequency response of fabricated SAW sensor (a) 20 μm pitch, 5 μm electrode width (b) 20 μm pitch, 6 μm electrode width (c) 24 μm pitch, 7 μm electrode width.....	74
Figure 53 Schematic of sensor position in the test chamber.....	76
Figure 54 Internal reflection in (a) Single electrode IDT (b) Double electrode IDT.....	77
Figure 55 Simulated frequency response for sensor with 24 μm pitch and 7 μm electrode width (a) with low-reflection boundaries (b) without low-reflection boundaries.....	79
Figure 56 Sensor frequency response after exposed to mercury vapor.....	81
Figure 57 Sensor frequency response after heating.....	81

CHAPTER ONE: INTRODUCTION

Mercury is a heavy metallic element that is liquid at room temperature and atmospheric pressure. The discovery of mercury can be dated back to 1500 B.C. in Egypt[1]. It was known and used for different purposes in ancient cultures like Greece, Rome, and China. For example, ancient Chinese people used mercury as an elixir for immortality[2]. However, it is known today as a highly-toxic material. Mercury is applied in diverse areas. It conducts electricity like common metals, forms alloys with most other metals and is sensitive to temperature and pressure changes. In daily life, some thermometers are made of mercury, which uses its volume change due to temperature change. It is also used in repairing dental caries and medicines. Mercury is a very important component for the electrical industry and chemical industry. In electrical industries, mercury can be made into switch using its conductivity and liquidity. Gaseous mercury is used to build fluorescent lamps. In chemical industries, mercury is used as a catalyst. However, the toxicity of mercury makes it a restricted material in all areas. Though the usage of mercury is decreasing gradually, the detection of mercury is very necessary.

Surface acoustic wave (SAW) sensor is a kind of sensor using the changes in resonant frequency or SAW velocity due to the sensing element properties change when it contact with the analyte.

In this work, a SAW mercury sensor with interdigital transducers (IDT) acts as the

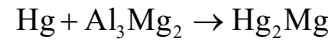
sensing element was studied. Commonly used mercury detection methods and the previous work done in LMST is discussed in this chapter. Chapter 2 discusses the theory of surface acoustic wave sensor. Chapter 3 shows the design process of SAW sensor using FEM simulation, including simulation models and results. Chapter 4 shows the fabrication process of the SAW sensor and the tests in this work. Chapter 5 presents some test results and discussion. Chapter 6 summarizes the findings of this work and discusses some possible directions for future work.

1.1 Motivation of This Work

1.1.1 Negative effect of mercury in industries

Mercury is mostly contained in earth's crust. During the mining and refining process of the petroleum industry, mercury is a very common contamination with huge negative effects in various ways[4]. The first and the one may cause most severe consequence is the corrosion of the components, mostly aluminum parts. Aluminum components are frequently used in petroleum industries, for example, the aluminum heat exchangers for the gas separation process. During the gas separation process, the mercury vapor mixed in the crude oil may condense to liquid phase mercury, which would cause damage to the heat exchanger due to liquid metal embrittlement (LME) and amalgam corrosion. The liquid metal embrittlement is more likely to affect aluminum-magnesium alloy, for instance, Al_3Mg_2 . The mercury would react with the

Al_3Mg_2 in grain boundaries and form a Hg-Mg compound.



The compound is insoluble in mercury thus its formation causes a crack that would propagate along the grain boundaries. [5-7] This process is shown in Figure 1.

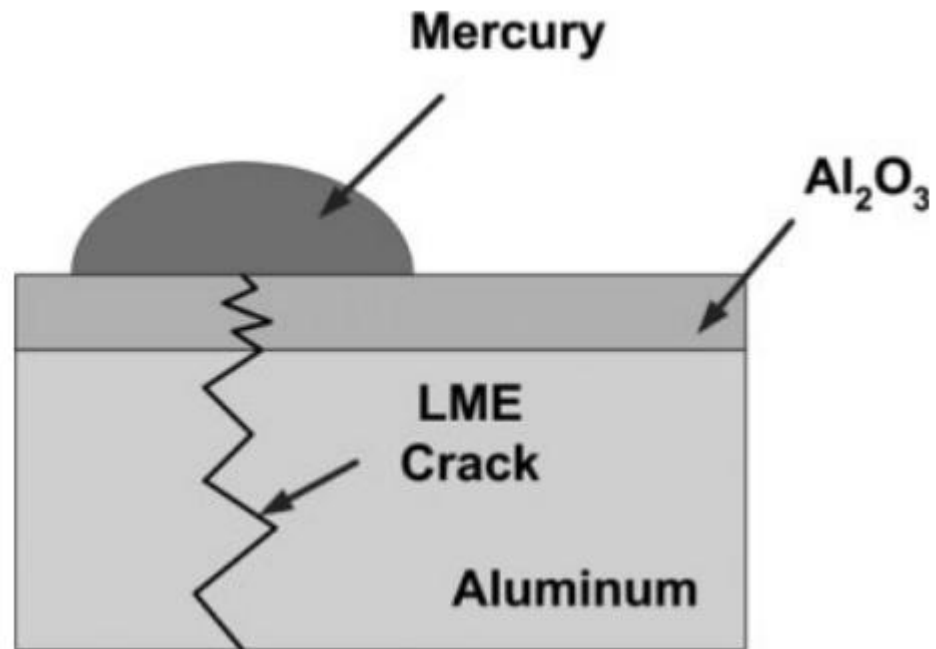
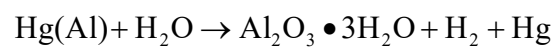
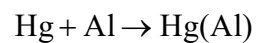


Figure 1 Schematic of LME[8]

Another reason for the corrosion of aluminum parts is amalgam corrosion. When aluminum alloy contacts with mercury, it would be dissolved. The mechanism of the reaction is[8]:



The reaction forms a cycle, so a small amount of mercury may cause severe corrosion. The reaction schematic is shown in Figure 2.

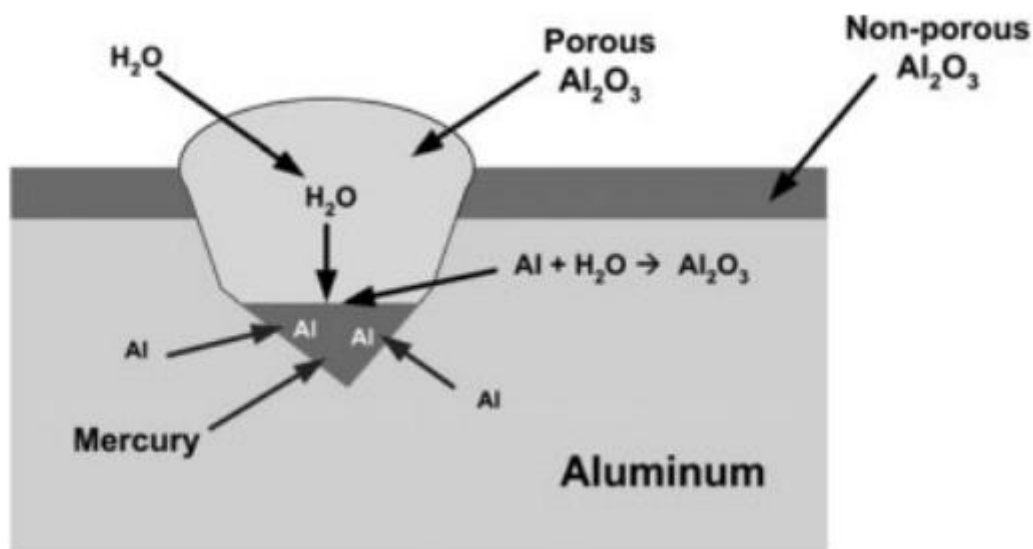


Figure 2 Schematic of amalgamation corrosion[8]

These reactions may lead to the failure of the exchanger and cause pressure loss, which may lead to accidents. On January 19, 2004, the Skikda gas-liquefaction plant in Algeria exploded killing 27, and injuring 72[9]. This accident resulted from the leak of liquefied natural gas (LNG) vapor from heat exchanger, which led to cloud explosion. This leak is believed to have been caused by liquid metal embrittlement. Another example is the Moomba gas plant fire on January 1st, 2004, which was confirmed to be due to LME in an aluminum vessel[10]. Mercury can also deactivate hydrogenation catalysts used during the mining/refining process, which not only would influence the working efficiency but also increase the cost. And as contamination, mercury lowers the

product's quality.

1.1.2 The health impact of mercury

Mercury poses a severe health risk to the refinery workers. Mercury can evaporate easily at room temperature, so mercury vapor is produced easily during the refining process. Mercury vapor can be absorbed very easily through lung tissue compared to food or drink, which makes mercury vapor more dangerous. Experiments show that 75-85% of inhaled mercury vapor would be absorbed by the human body[5].

Long-term exposure to low concentration mercury vapor can cause nervous system damages lead to symptom include tremors and impaired cognitive skills[5]. Fawer et al.(1983) measured intention tremor in workers exposed to low concentration mercury vapor (time-weight-average of 0.026 mg/m^3) for a long period (average 26 years). A significant difference was observed, the frequency of tremors in exposed workers was higher than referents[11]. Piikivi and Tolonen (1989) studied electroencephalograms (EEG) of 41 workers exposed to low concentration mercury vapor (around $2.5 \text{ }\mu\text{g/m}^3$ in air) for long term (mean 15.6 years). They found compare to the referents, the exposed workers had significantly slower and attenuated EEGs[12]. Piikivi and Hannien (1989) studied subjective symptoms and psychological performances in 60 workers exposed to mercury vapor for a long term. The exposed workers were found to have a significantly increased memory disturbance and sleep disorders compare to referents[13].

Neurological signs and symptoms, impaired performance in mechanical and visual memory tasks and psychomotor ability were also observed[14,15].

Some more serious symptoms such as dyspnea, impairment of pulmonary function to kidney and liver failure can also happen, and acute exposure can even cause death[5]. Kazantzis (1962) reported 4 cases of heavy albuminuria and renal failure caused by mercury exposure[16]. Tubbs et al. (1982) reported cases of proteinuria and glomerulonephritis in chemical plant workers[17]. Jaffe et al. (1983) reported acute renal failure in an eight-month-old child due to element mercury exposure[18]. Taueg et al. (1992) reported cases of 4 adults died 11–24 days after acute exposure[19].

All previous researches show that even tiny amount of mercury has the potential to cause severe damage to both industrial instrument and human health. Consequently, it is very necessary to have an effective way to detect low concentration element mercury vapor.

Mercury vapor existing in the petroleum industry is usually very low concentrated ($1 \mu\text{g}/\text{m}^3$ level), making it hard to be detected with common detection methods. So the objective of this work is to develop an accurate and efficient way to detect low concentration element mercury vapor on site.

1.2 Commonly Used Methods For Mercury Vapor Detection

1.2.1 Cold vapor atomic absorption spectroscopy (CVAAS)

Cold vapor atomic absorption spectroscopy (CVAAS) is one of the most accurate ways to determine the concentration of mercury vapor presently. For inorganic mercury, it can reach a detection limit around 200 ng/m^3 [20]. The working principle of CVAAS is that according to Beer-Lambert Law, different element atoms can absorb the characteristic wavelength of light. The amount of light that's absorbed is proportional to the concentration of the analyte in the sample. So by measuring the attenuation of the light, the concentration of the analyte can be determined[21].

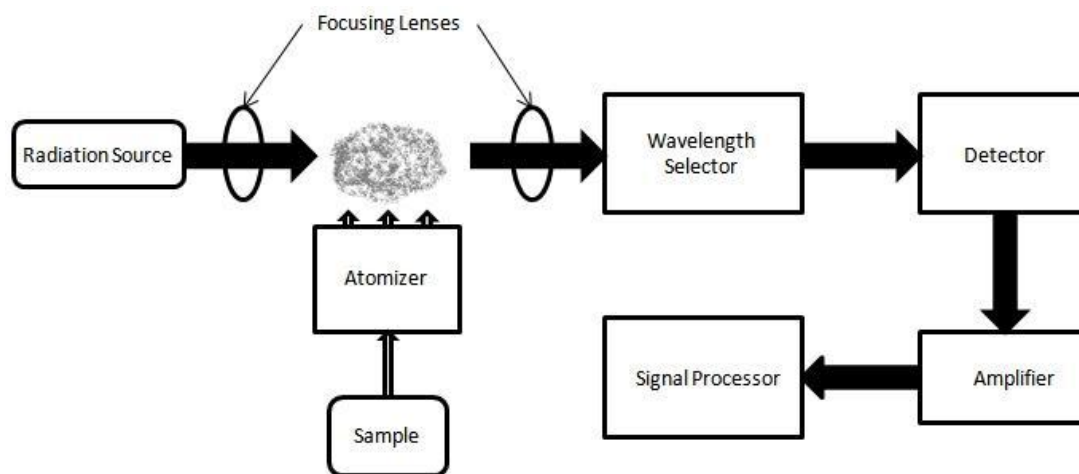


Figure 3 Schematic of CVAAS

Figure 3 is a schematic of CVAAS. The main component includes radiation source, usually a UV light, sample cell that contains the analyte and detectors to detect the attenuation of incident light. The light generated by the UV light goes through the sample cell to the detector. By comparing the signal, detector received with the original

sign the attenuation can be determined. Thus the concentration can be detected.

CVAAS is a very accurate method for element mercury detection. However, this approach has some significant drawbacks. For the case of on-site detection, the most important one is very long analysis times and complex steps where specially trained personnel required[22].

1.2.2 Cold vapor atomic fluorescence spectrometry (CVAFS)

Another widely used detection method for mercury vapor is cold vapor atomic fluorescence spectrometry. Generally, the species that can be examined has two different electronic states, ground electronic state and excited state. Under normal condition, mercury atom is in the ground electronic state. When the mercury atom is excited by absorbing a photon, it goes into the excited electronic state. But this state won't last long; the atom will drop down back to ground electronic state again and a photon will be emitted in this process. Because there are no vibrational energy levels in atom species, the photon emitted is usually at the same energy level as the incident radiation. This emission produces fluorescence, and by measuring the amount of fluorescence, the concentration of mercury can be determined[23,24]. The structure of CVAFS is similar to CVAAS. The difference is the detector, usually, a photomultiplier is placed perpendicular to the direction of incident light to avoid the interference.

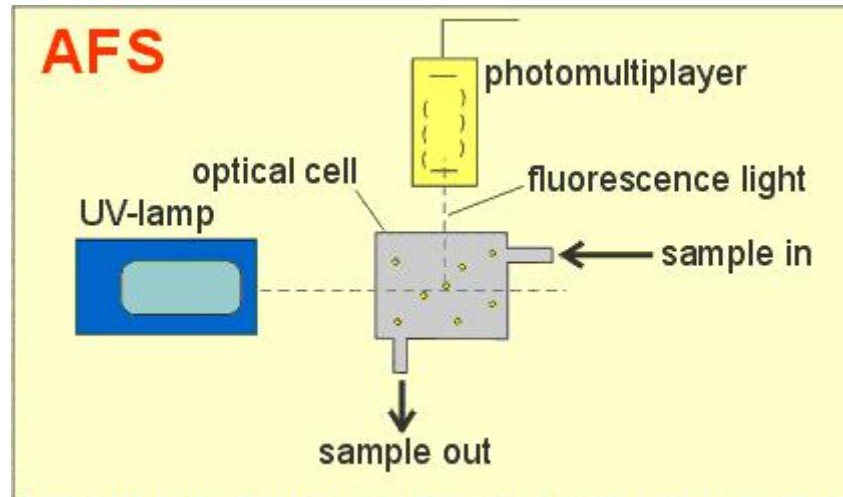


Figure 4 Schematic of CVAFS[25]

CVAFS has similar detection level and drawbacks with CVAAS. It's very accurate, but not suitable for on-site detection[26].

1.2.3 Microcantilever sensor.

Microcantilever sensor is a relatively new method for mercury detection. There are two kinds of microcantilever sensors with similar structure. Figure 5 shows the structure of a microcantilever array.

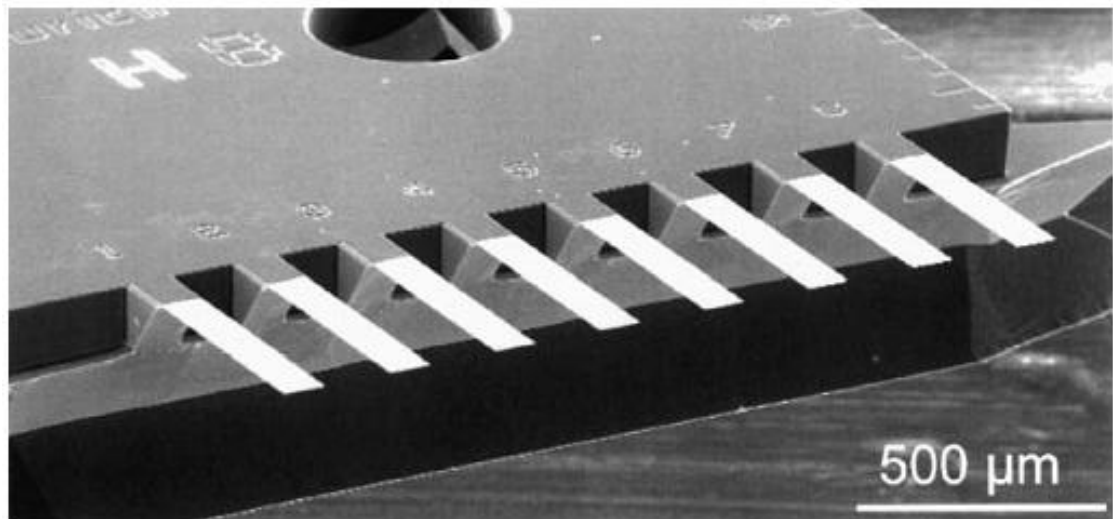


Figure 5 Microcantilever array[27]

For the case of mercury detection, the upper side of the microcantilever is coated with gold, which is known to have a particular affinity with mercury[28]. When mercury vapor contacts the thin gold film coated on microcantilever, the Hg atoms will be adsorbed on the surface of the gold film. The mass change causes a change in the resonance frequency and the bending of the microcantilever. The mercury concentration can be determined by measuring either of these two changes[29]. The deflection sensing uses an optical system shown in Figure 6. A beam of light is focused onto the tip of the cantilever; the reflected light is measured by a detector. When the cantilever bends, the reflection angle changes, and this angle change can be converted to the concentration of mercury vapor[28]. The measurement of resonant frequency change can be realized by nanoscope probe[29].

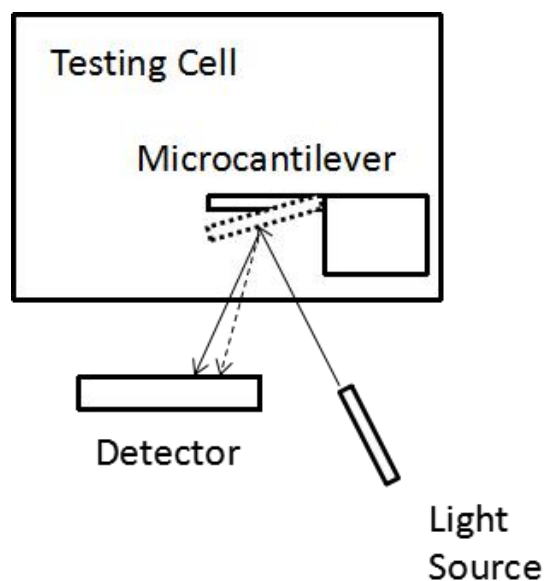


Figure 6 Schematic of deflection microcantilever sensor.

The microcantilever sensor has been used in on-site detection, but the fabrication process is relatively complicated.

1.2.4 Surface plasmon resonance sensor

Surface plasmon resonance sensor is used in various areas. It utilizes the surface plasmon resonance phenomenon as the sensing mechanism. Surface plasmon resonance is a charge-density resonant oscillation happens at the interface between a negative permittivity material and a positive permittivity material. The resonance wave is excited by incident light. The resonance frequency is very sensitive to the change of optical properties of the two materials. Thus the chemical reaction near or on the surface of the sensor can be measured through the changes in the resonance frequency[30,31]. For low concentration mercury sensing, gold nanoparticle is used as sensing material the adsorption of mercury can lead to optical properties change and in nanoparticle form the optical property change can be followed by simple methods. Due to surface plasmon resonance gold nanoparticles exhibit absorbance peak at the resonance frequency, when mercury contact with gold nanoparticles the optical property will change and there will be a shift in absorbance peak. By measuring the peak shift, the concentration of mercury vapor can be determined[28,31]. The surface plasmon sensor can reach a detection limit of $1\mu\text{g}/\text{m}^3$ for mercury vapor detection but it doesn't fit the requirement of on-site sensing[31].

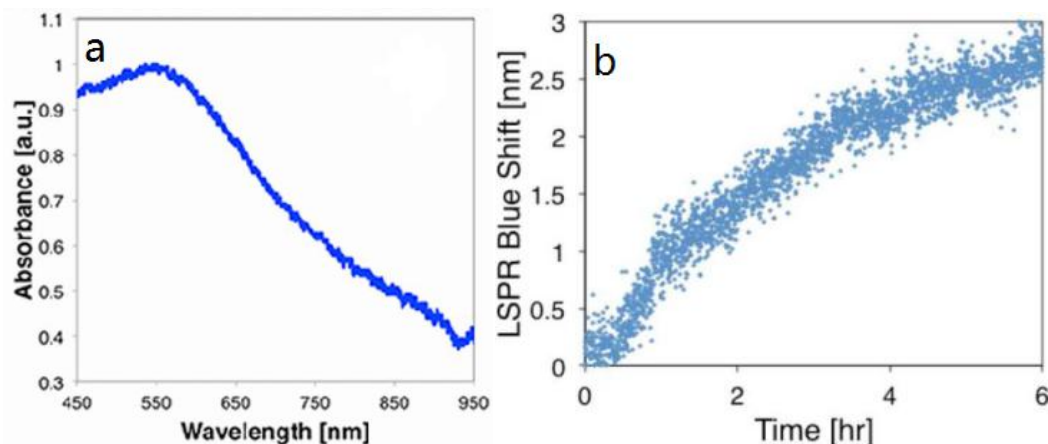


Figure 7 (a) A absorption figure of gold nanoparticle film on quartz. (b) The trace of peak shift during exposure to mercury vapor[31]

1.2.5 Resistivity (conductivity) sensor

Resistivity sensor or conductivity sensor is a sensing method that's thoroughly studied. The sensing principle is based on the resistivity (conductivity) change when gold thin film adsorbs mercury vapor. During the adsorption, the electrons in mercury transfer into gold film and cause electron density changes in gold film. And the resistivity increase is proportional to the mercury surface concentration before saturation[32]. The measurement of resistivity is based on a simple structure, Wheatstone bridge. Figure 8 is a resistivity mercury sensor based on Wheatstone bridge structure. Two opposite resistors are covered by photoresist as reference and two without photoresist as sensing element. Theoretically this structure can eliminate the influence of temperature. The detection limit of resistivity sensor can reach $4 \mu\text{g}/\text{m}^3$ by using a special readout procedure[32]. Our group did some work based on the resistivity sensor which will be discussed in the following section..

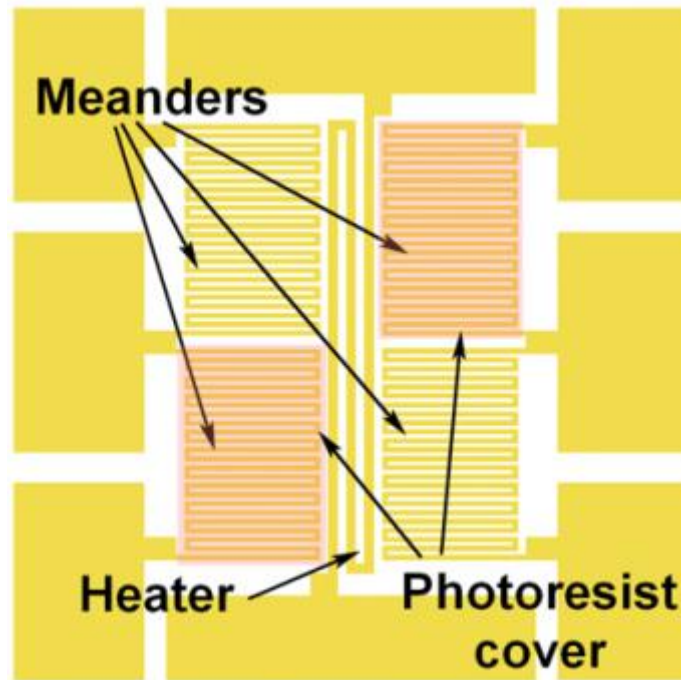


Figure 8 A resistivity based mercury sensor design[32]

1.2.6 Surface acoustic wave(SAW) sensor

Surface acoustic wave sensor is first used in mercury sensing in the 1990s' and it have a lot of potential for repeatable, low concentration mercury vapor sensing[33]. Surface acoustic wave is a mechanical wave that propagates through the surface of an elastic material. The surface acoustic wave is very sensitive to characteristic changes to the surface. The most common structure of a SAW sensor is shown in Figure 9. There are two pairs of interdigitated transducers(IDT) working as signal input and output, respectively. They are patterned on a piezoelectric substrate. When applying opposite voltage separately on the pair of IDTs on the input side, the inverse piezoelectric effect

would cause vibration and generate surface acoustic wave.

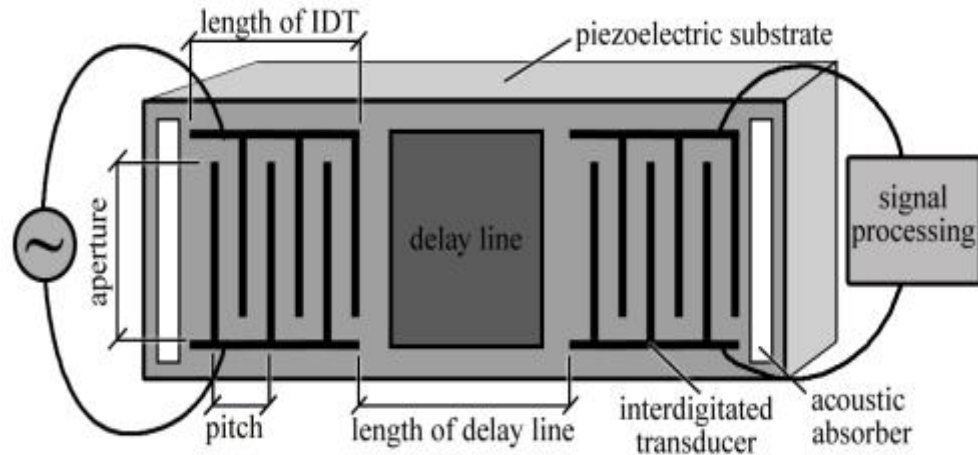


Figure 9 Schematic of a typical SAW sensor structure [34].

When the surface acoustic wave travels through the delay line and reaches the output port, it would generate electric signal again by piezoelectric effect. The property change of the delay line will affect the propagation of surface acoustic wave, causing changes in the output signals such as phase change and propagation speed change. In this fashion, the delay line works as the sensing element, and it is made with materials whose physical/chemical properties would change in response to the changes in the surrounding environment. These property changes can be finally reflected by the change in output wave properties. For SAW-based mercury detection, gold would be the suitable sensing material. The adsorption process between mercury and gold changes the density of delay line. The SAW sensor design of delay line act as sensing element has been studied by many researchers.

For low concentration mercury detection, a novel design is reported. K. M. Mohibul Kabir et al. [35] reported a SAW based selective mercury vapor sensor using IDTs as sensing element. Instead of using gold delay line to react with mercury, gold IDTs are used. The resonant frequency of the SAW sensor changes when gold electrodes adsorb the mercury vapor. The detection limit of this design can reach a level under $10 \mu\text{g}/\text{m}^3$ with a good selectivity (95%). And the fabrication process is relatively straightforward compare to other methods[35]. Thus the design of SAW sensor with gold electrodes as sensing elements is applied in this work.

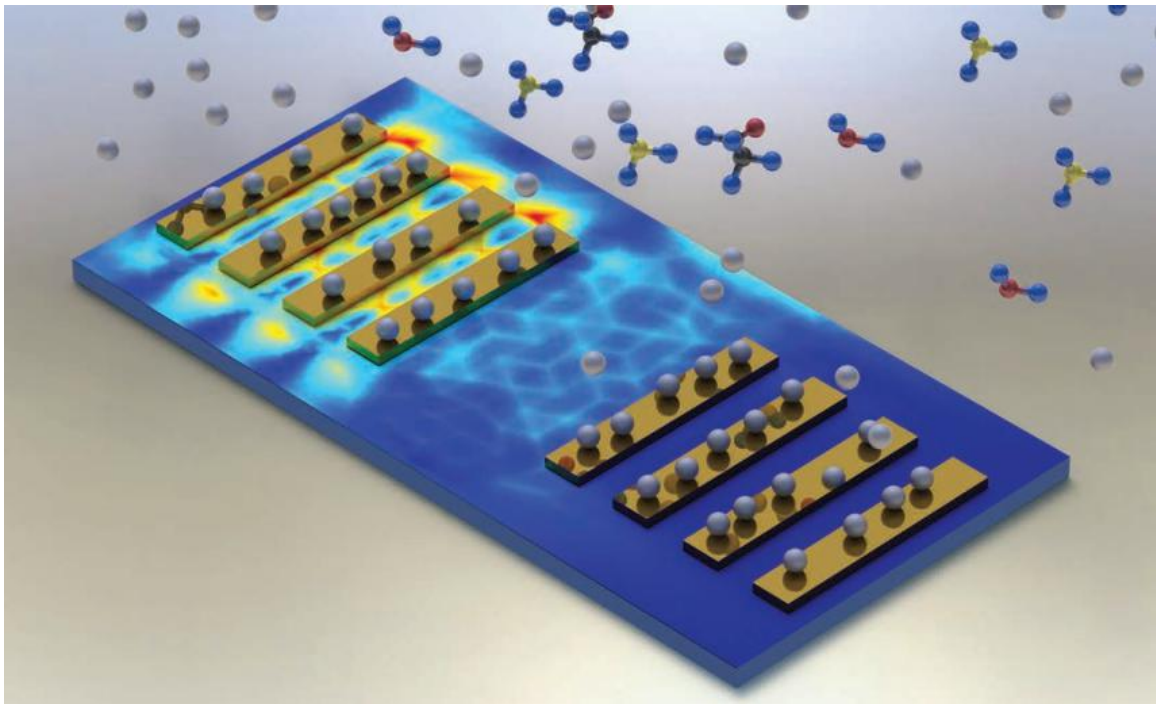


Figure 10 Schematic of SAW sensor with gold IDTs as sensing element[35]

1.3 Previous Work

Experiences have been done in our lab with the resistivity (conductivity) sensor. Gold resistors were used as sensing elements and different versions of sensors were developed. The design of sensor version 1 is shown in Figure 11 and experiment result is shown in Figure 12. There are four gold resistors on the sensor form a Wheatstone Bridge; two opposite resistors perform as reference and other two as sensing element. According to lecture[32], the resistance increase should be or very close to linear before saturation.

Figure 12 (a) and 12 (b) are the results of reference resistor measurement and testing resistor measurement, respectively. It can be observed from Figure 12 that during the testing, the result curves are almost identical to each other, there's no sign of mercury detection. The variation of resistance is caused by temperature change, and it was quite large, which has a significant negative effect on the sensing process since the measurand is the change of resistance.

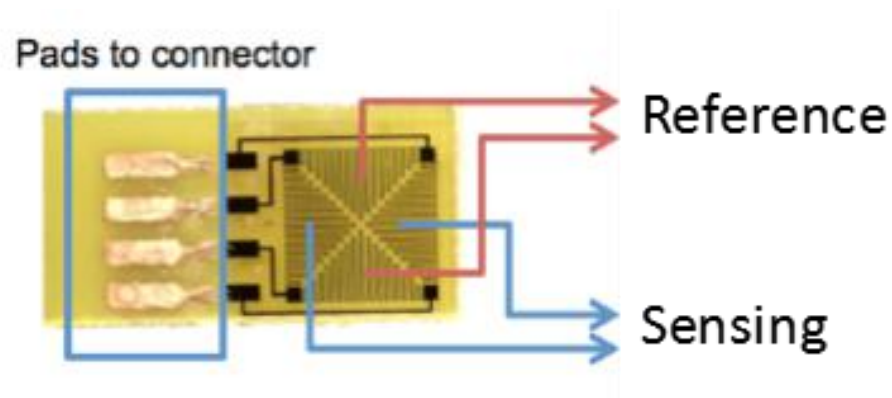


Figure 11 Resistivity sensor version 1

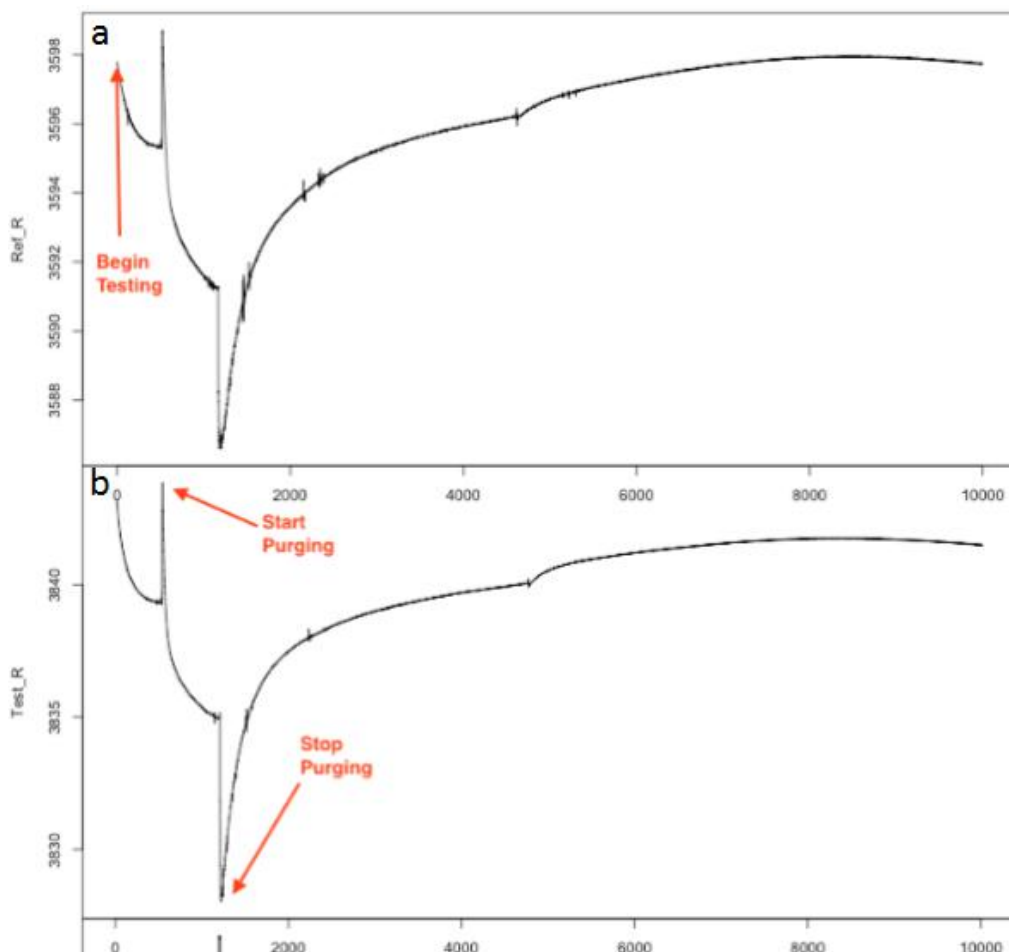


Figure 12 Result of sensor version 1 test (a)reference resistor measurement (b)testing resistor measurement

No sign of mercury in this experiment. The reason might be the measured mercury concentration was too low to be detected. Then a long time (10 hours) exposure test was done to observe the effect of gold thin film contact with mercury vapor. The test concentration of mercury vapor is 40 ng/m^3 . SEM pictures were taken to see if there's any mercury adsorption on gold surface. Figure 13 (a) and (b) are the picture of gold surface before exposure and gold surface after 10 hours of mercury vapor exposure, respectively. There are no distinct features between the two pictures. No sign of

amalgamation. The reason for this result may be the concentration of mercury vapor generated by the mercury generator is too low (40 ng/m^3).

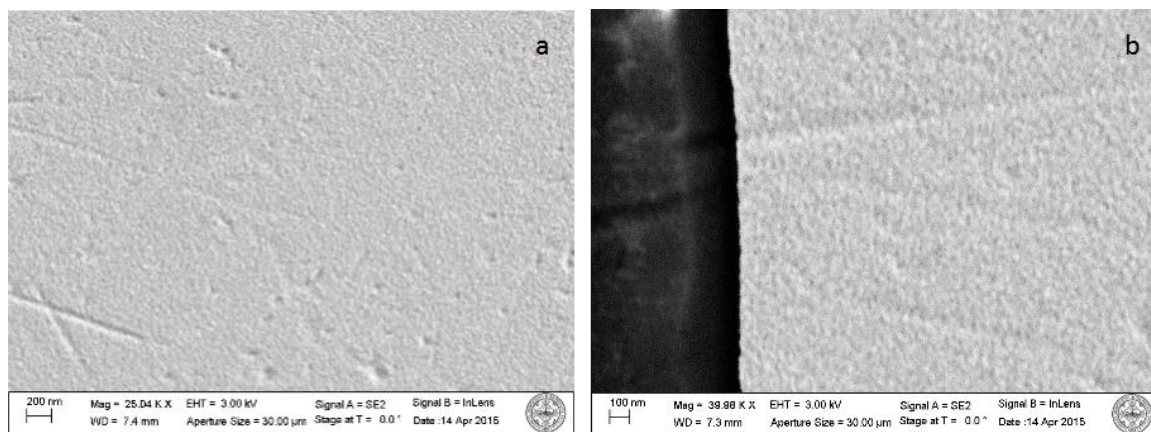


Figure 13 SEM results (a) gold surface before exposure (b) gold surface after 10 hours exposure

Except for the low mercury vapor concentration, the temperature dependence is also a big problem. Thus the sensor version 2 was built, a temperature sensor was added on the chip. First, two long run experiments were carried out. Experiment 1 was 3 days exposure to 40 ng/m^3 concentration; experiment 2 was 4 days exposure to 40 ng/m^3 . Figure 15 (a)(b) are the resistance measurement result of experiment 1 and 2, respectively. It can be seen that the resistance depend heavily on temperature. Figure 15 (c)(d) are resistance difference of experiment 1 and 2. The results of resistance difference are conflicted. As shown in Figure 15 (c), the resistance difference is negative which means the resistance was decreasing during the test but in Figure 15 (d) the tendency of resistance difference is increasing. Nothing can be concluded from these results. Besides, the experiment results are not repeatable.

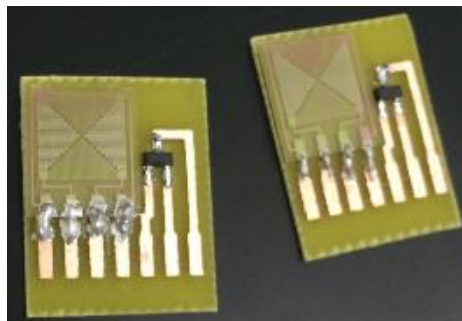


Figure 14 Sensor version 2 with temperature sensor

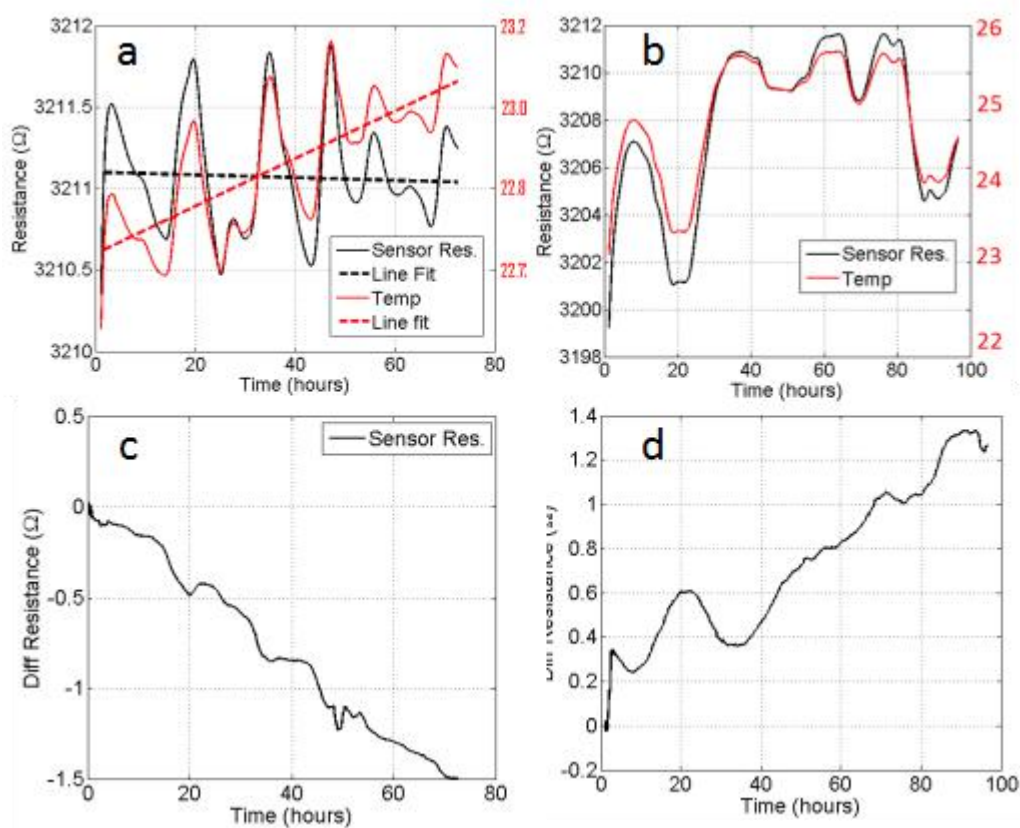


Figure 15 (a) Resistance measurement result of 3 days 40 ng/m^3 exposure (b) Resistance measurement result of 4 days 40 ng/m^3 exposure (c) Resistance difference of 3 days 40 ng/m^3 exposure (d) Resistance difference of 4 days 40 ng/m^3 exposure

However, some good results were also achieved with this sensor. Figure 16 (a) (b) are resistance measurement and resistance difference under mercury vapor concentration 40 ng/m^3 , 2 L/min with sensor version 2, (c) (d) are resistance measurement and

resistance difference under 20ng/m^3 , 4L/min with sensor version 2. The resistance measured is still heavily dependent on temperature, but the tendencies of resistance difference are both increasing, very close to linear. These results are consistent with lecture, but the experiments cannot be repeated.

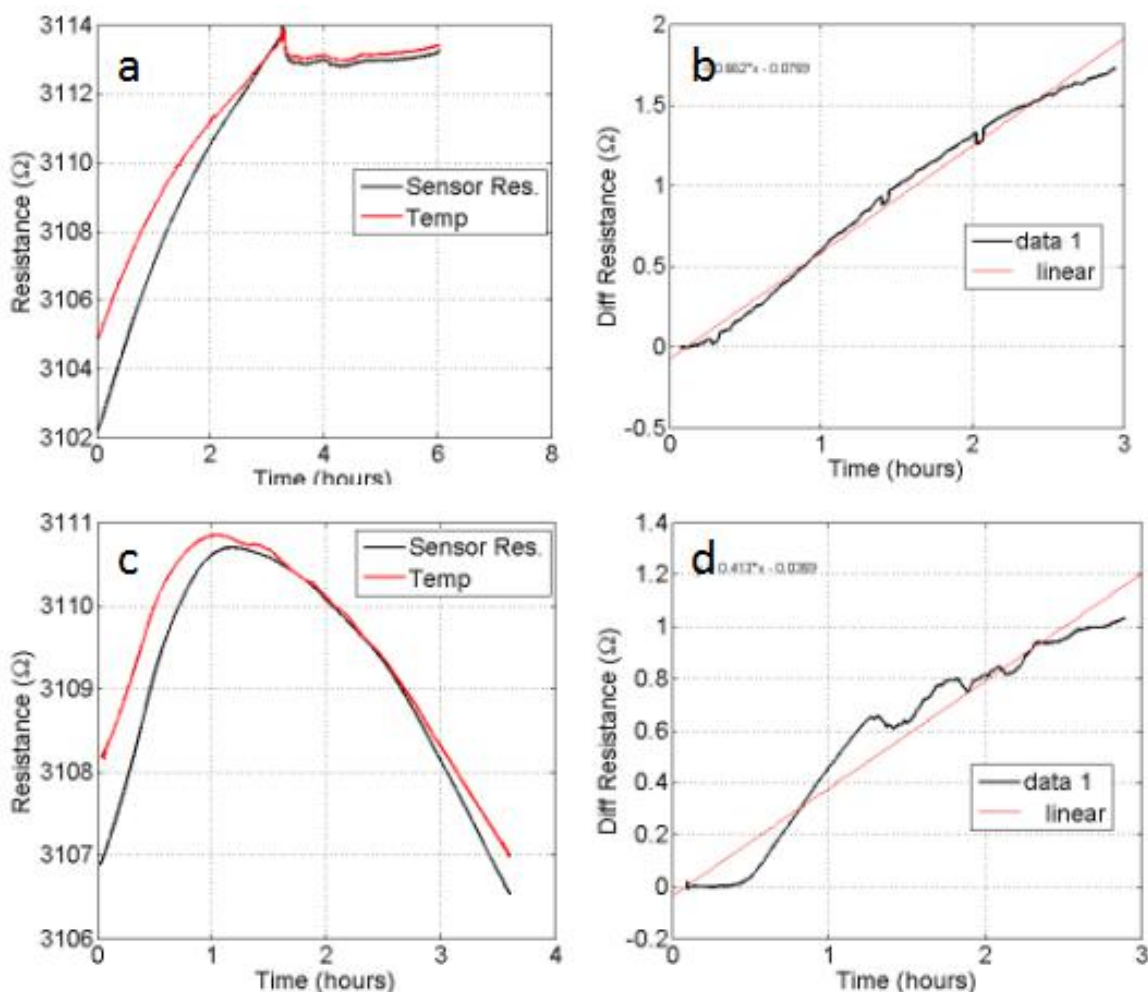


Figure 16 (a) Resistance measurement under mercury vapor concentration 40ng/m^3 , 2L/min with sensor version 2 (b) Resistance difference under 40ng/m^3 , 2L/min (c) Resistance measurement under 20ng/m^3 , 4L/min with sensor version 2 (d) Resistance difference under 20ng/m^3 , 4L/min

The major problems encountered with experiment 1 and 2 include the low

concentration of mercury vapor generated by mercury generator which leads to very little response or even no response and the performance of the sensor was severely influenced by temperature variation. To increase the sensitivity, a new sensor design was applied. The sensor was built as a Wheatstone bridge but used as a resistive sensor as shown in Figure 17. And to compensate the effect of temperature change, sensor with temperature reference was built. But no meaningful result was achieved with these sensors. The major problem was the tendencies of resistance difference were not only disagree with theoretical tendency but even not consistent with each other. This could be attributed to the mercury vapor concentration was too low, but the existence of mercury was in doubt.

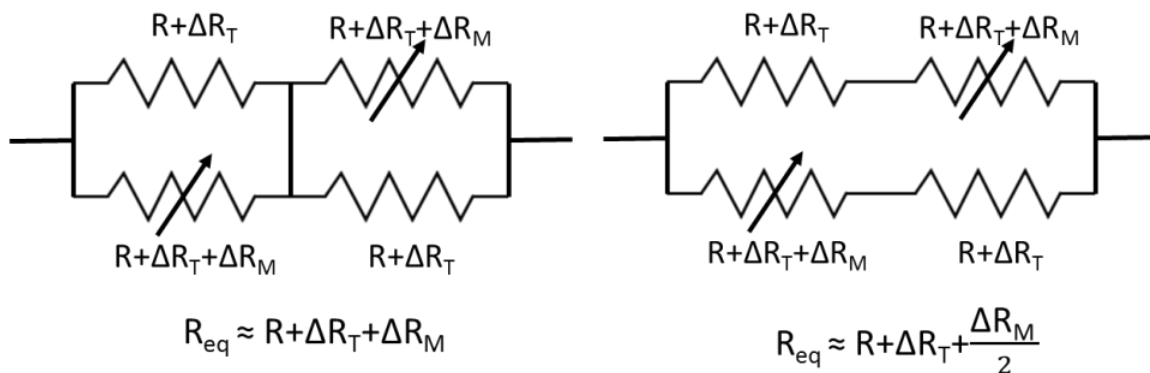


Figure 17 Comparison between resistive sensor(left) and Wheatstone bridge(right)

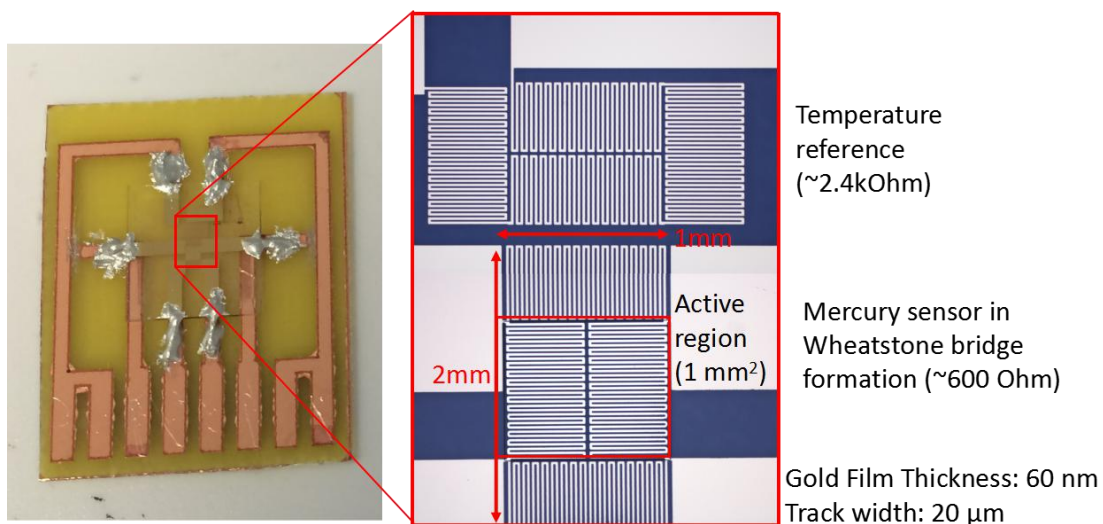


Figure 18 Wheatstone bridge sensor with temperature reference

A selective filter coating was applied on the sensor. Hexadecanethiol can act as selective filter to eliminate the influence of interference, thus the existence of mercury vapor can be tested[36]. A 120 hours long run test was carried out, normalized output result and output difference are shown in Figure 19 (a) (b), respectively. From the output difference, it can be observed though the change is very small, the tendency of change is increasing. This can indicate the existence of mercury vapor.

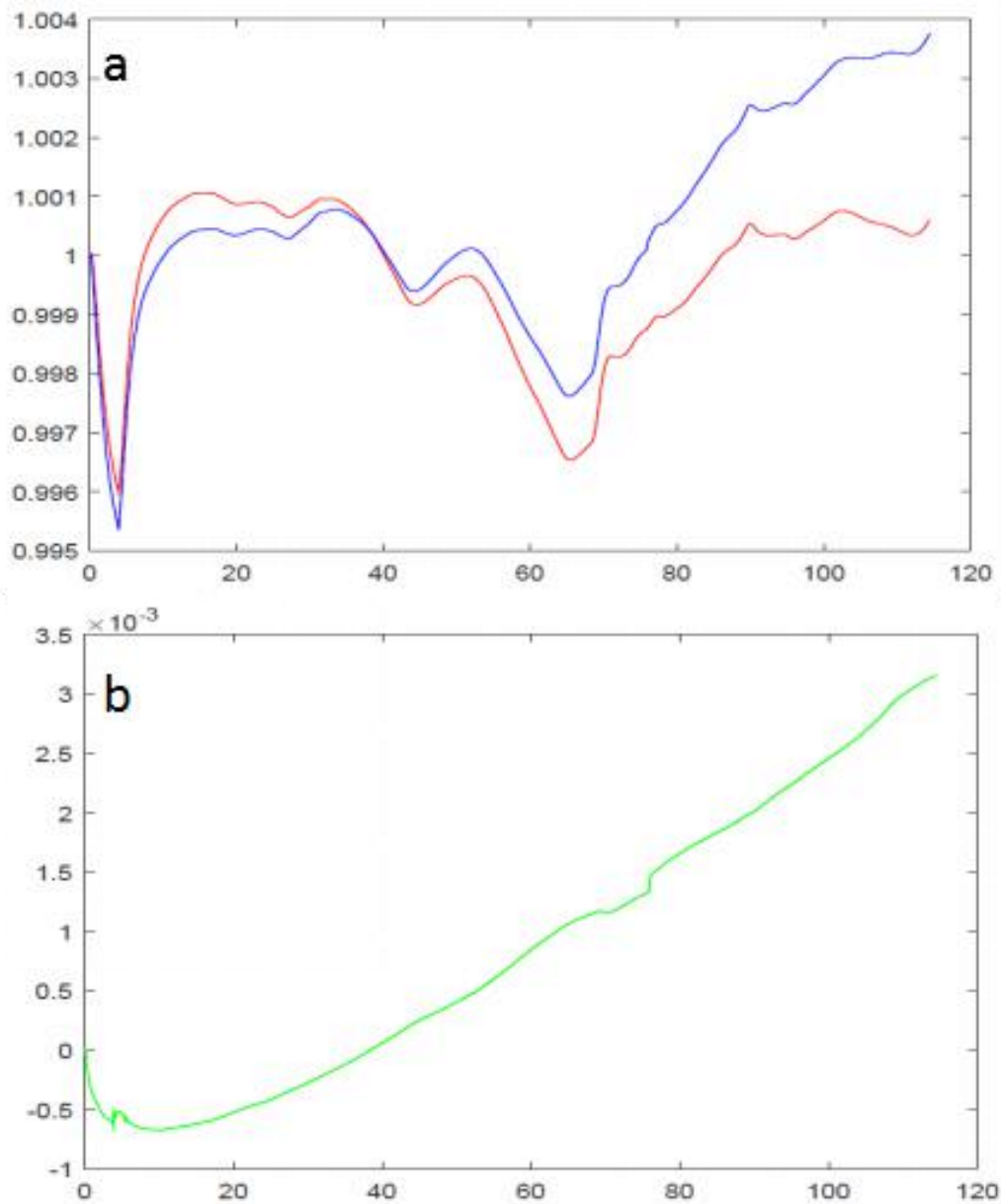


Figure 19 Normalized test result of selective filter coated sensor (a)sensor output, blue curve is mercury sensor output, red curve is temperature reference. (b) Difference of two outputs.

From the results of previous work, a few conclusions can be made. First, the mercury generator did generate mercury vapor, but of very low concentration. Second, the resistivity sensor was not capable of sensing such low concentrated mercury vapor. In

the last experiment with selective coating, the existence of mercury vapor was confirmed. Meanwhile, a 120 hours exposure only resulted in a 3% change of the resistivity. The output of resistivity sensor was heavily influenced by the temperature, such a small change caused by mercury vapor can hardly be distinguished, let alone the requirement of on-site sensing. Furthermore, the time needed to reach such a response is too long.

Compare to previous work, a SAW sensor could bring low detection limit while maintaining good selectivity and temperature stability. In K. M. Mohibul Kabir et al.'s work[35], SAW sensor showed a good temperature stability because the ST-cut quartz substrate has extremely low temperature coefficient and the resonance frequency of the sensor won't be influenced by temperature. This can solve the problem of resistivity sensor fundamentally. And the selectivity of the sensor was around 95% with a good repeatability[35]. Without the efforts to maintain stable and selective the fabrication of SAW sensor could be easier than resistivity sensor in previous work. The detection limit reported is around $10 \mu\text{g}/\text{m}^3$ level[35]. Though this is not as low as the goal of this work, it is believed the detection limit can be improved, and a finite element method model was built to studied the sensor performance in chapter 3.

**CHAPTER TWO: THEORETICAL MODEL OF SENSING MERCURY VAPOR
WITH SURFACE ACOUSTIC WAVE (SAW) SENSOR**

2.1 Surface Acoustic (Rayleigh) Wave

In an elastic medium, the displacement of a single element will cause a disturbance propagate through the entire medium like in a distributed mass-spring system. An elastic wave arises when elastic and inertial forces are distributed, very similar to a mass/spring system oscillate[37]. The waves propagate in the elastic medium includes bulk longitudinal wave, surface (Rayleigh) wave and bulk transverse wave. Figure 20 is a schematic of different waves.

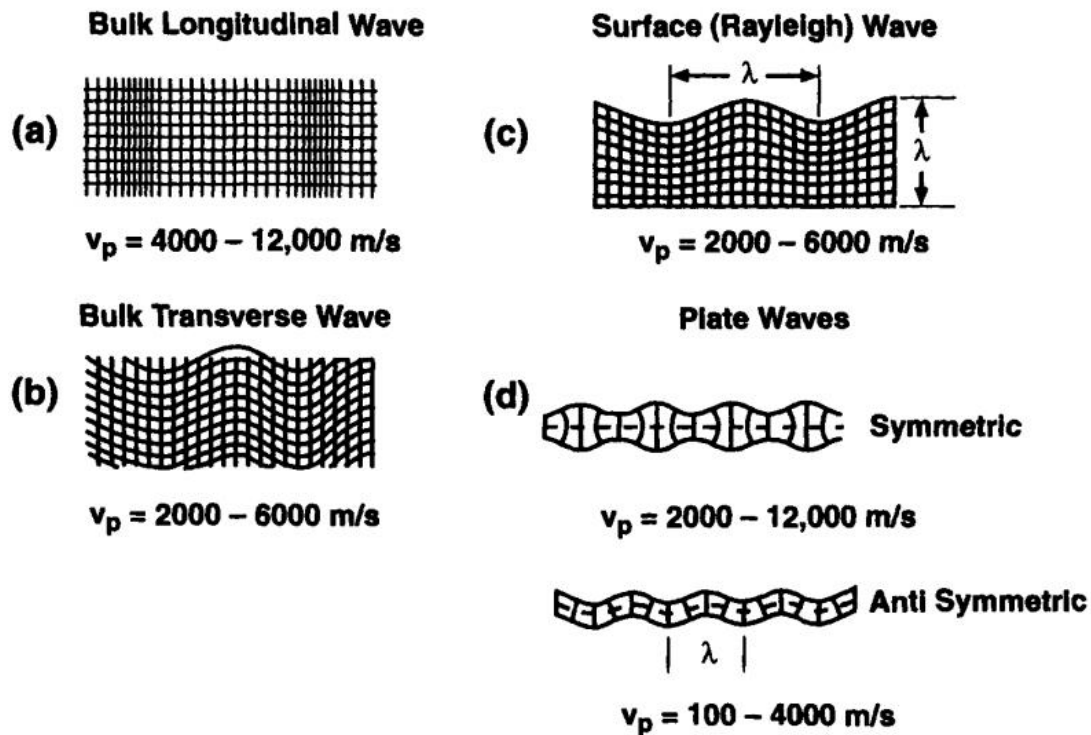


Figure 20 (a)Bulk longitudinal (compressional) wave (b)Bulk transverse (share) wave (c) Surface acoustic (Rayleigh) wave (d)Waves in solid plates [37]

Among these waves, surface acoustic wave (SAW) is used as the sensing mechanism in SAW sensor. It is an acoustic wave that the component of the wave is perpendicular to the surface it travels along. Surface acoustic wave was first discovered and explained by Lord Rayleigh in 1885[37]. As shown in Figure 20, the depth surface acoustic wave propagate in the medium is around 1 wavelength, which means the majority of the energy of the surface acoustic wave is contained within one wavelength depth from the surface of the material. This makes surface acoustic wave very sensitive to the change of medium properties, and it can propagate much farther than other waves without significant attenuation[37].

2.2 The Piezoelectric Effect

The piezoelectric effect was discovered by Pierre and Paul-Jacques Curie in 1880. They found that some single crystals of certain materials can generate surface charge when external force was applied to it. And on the contrary, applied voltage will result in mechanical deformation. So piezoelectric materials can behave as both sensors and actuators[38].

Before the external force is applied, the charges in the crystalline unit cell of piezoelectric materials are randomly orientated and the charges canceled out, the unit cell is neutral as a whole. When an external force is applied to a piezoelectric material, it will cause the movement of centers of net positive and negative charges within the crystalline

unit cells. The charges are separated which results in an electric field within the piezoelectric material[38]. That's the principle of piezoelectric effect and vice versa for inverse piezoelectric effect.

The relationship between strain and electric field can be expressed in terms of these two equations[37]:

$$T_i = c^E_{ij} S_j - e_{ij} E_j \quad (1)$$

$$D_i = \varepsilon^S_{ij} E_j + e_{ij} S_j \quad (2)$$

These are the piezoelectric constitutive relations, in which e_{ij} are the piezoelectric stress constants, E_i is the electric field components, D_i are the electrical displacement components, and ε_{ij} are the permittivity constants[37]. The characteristic of convert electrical signal and mechanical strain makes piezoelectric material a perfect fit for SAW sensor.

2.3 Adsorption of Mercury on Gold

The key factor of mercury sensing based on mass or density changing is that it can be adsorbed by gold. The adsorption mechanism of mercury on gold is rather complex. An adsorption model studied in [39] is shown in Figure 21.

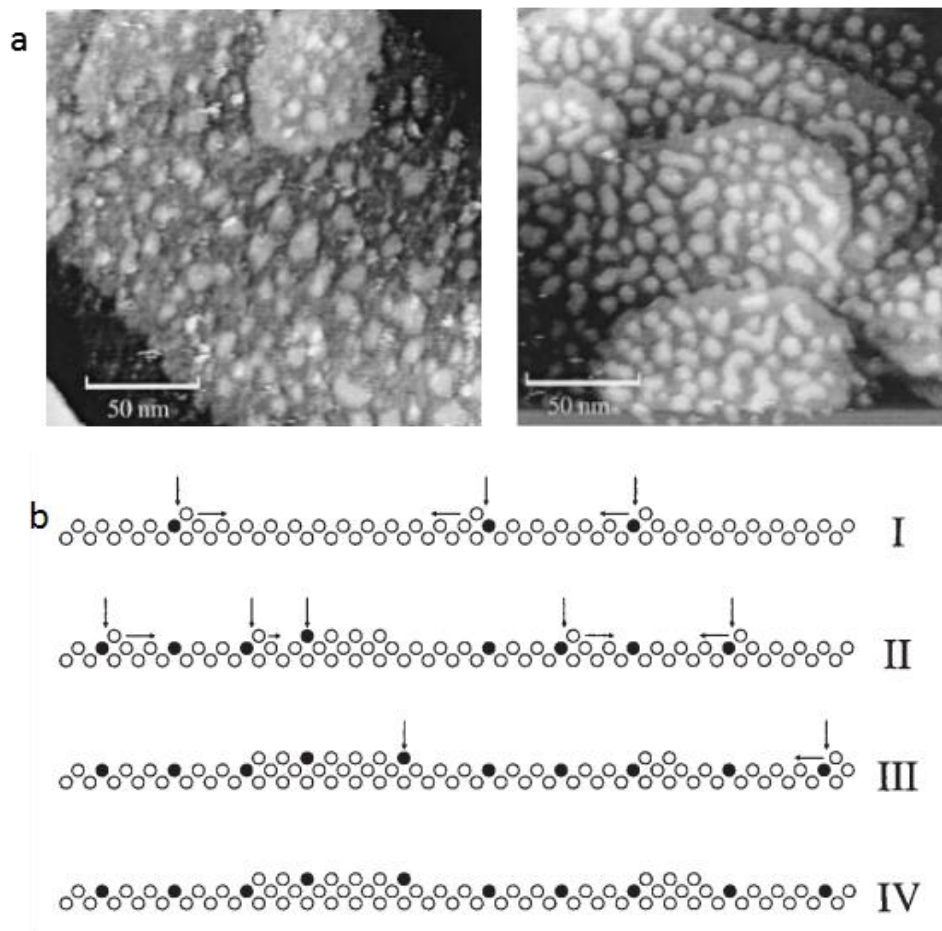


Figure 21 (a) Image of gold substrate exposed to 30 ng/L mercury vapor at room temperature (left) and 60°C (right) for 360 minutes (b) The adsorption mechanism of mercury on gold[39]

The adsorption process cannot be described as a simple layer-by-layer growth model. It is based on the surface exchange epitaxy which means the adsorbate atoms tend to replace the substrate atoms within the top atomic layer[40]. When mercury atom contact the gold surface, gold atoms from the first surface layer will be transferred onto the top of the layer as shown in Figure 21 (b) step I. These gold atoms form islands and number of these sites increases with the adsorption of mercury as Figure 21 (b) step II,III shows[39]. Finally all sites that free sites that place exchange can happen are filled and

the surface reaches saturation.

2.4 SAW Velocity (Frequency) Perturbation Theory

The common way to use surface acoustic wave as a sensing principle is to measure the change in SAW velocity (frequency) due to the change of the medium surface properties[37]. The resonance frequency of the SAW delay line can be calculated as [34]

$$f_0 = \frac{V_R}{P} \quad (3)$$

where V_R is the speed of surface acoustic wave, P is the length of pitch.

Hank Wohltjen[41] derived the change of SAW velocity to mechanical perturbation based on Auld's work[42] as

$$\frac{\Delta V_R}{V_R} = (k_1 + k_2) f_0 \rho h - k_2 f_0 h \left(\frac{4\mu}{V_R^2} \left(\frac{\lambda + \mu}{\lambda + 2\mu} \right) \right) \quad (4)$$

Where k_1 and k_2 are material constant related to the normalized particle velocity surface component, f_0 is the resonant frequency of the sensor, ρ is film mass density, in this work is the density of gold electrodes, h is the thickness of gold electrodes, V_R is the SAW velocity in the substrate material and λ , μ are lame constants of the gold thin film.

Besides, the shift of SAW resonant frequency is also caused by acoustic-electric perturbations expressed by Equation (5). [37,43]

$$\frac{\Delta V_R}{V_R} = \frac{-k^2}{2} \frac{1}{1 + \left(\frac{V_R \epsilon_\rho}{\sigma_{sh}} \right)^2} \quad (5)$$

In Equation (5) k^2 is the electro-mechanical coupling coefficient of the substrate material, ϵ_p is the effective permittivity of the whole structure and σ_{sh} is the sheet conductivity of the gold electrodes. From Equation (5), the acoustic-electric perturbation is proportional to the electro-mechanical coupling coefficient of the substrate. Thus the influence of acoustic-electric perturbation on frequency shift can be ignored by choosing a substrate material with low k^2 value such as ST-cut quartz ($k^2=0.11$)[35].

In case of resonant frequency change, the relationship between SAW velocity and resonant frequency is[42]:

$$\frac{\Delta V_R}{V_R} = \frac{\Delta f}{f} \quad (6)$$

So the frequency shift can be expressed in the form of

$$\Delta f = (k_1 + k_2)f_0\rho h - k_2 f_0^2 \rho h \frac{4\mu}{v_0^2} \left(\frac{\lambda + \mu}{\lambda + 2\mu} \right) \quad (7)$$

The mechanical stiffening effect is negligible for thin film[41] so Equation (7) can be simplified to

$$\Delta f = (k_1 + k_2)f_0\rho h \quad (8)$$

In terms of Equation (8) the frequency shift only depends on the changes in density and thickness of thin gold film. The frequency shift is proportional to the concentration of mercury vapor in the test sample because the density change of gold electrodes due to the amalgamation is proportional to the concentration of mercury vapor contact with

electrodes. [35] The substrate material was chosen as ST-cut quartz for its very low electro-mechanical coupling coefficient (0.11). In this way the acoustic-electric response can be ignored, the frequency change can be considered as the result of only density and thickness changes of the electrodes.

CHAPTER THREE: FEM SIMULATION AND DESIGN OF THE SAW SENSOR

In order to design a sensor that satisfies the $1 \mu\text{g}/\text{m}^3$ level detection limit, finite element method (FEM) was employed to study and optimize the factors that influence the sensor's sensitivity.

3.1 FEM Simulation Model Parameters And Boundary Conditions

The FEM simulations are done by COMSOL 5.2 Multiphysics. In order to save calculation time and lower the hardware requirement, a simplified 2D SAW sensor model was built. The model parameters are shown in Table 1. The structure of the SAW sensor model is shown in Figure 22. During the simulation parameters such as the electrode width was changed to study how the sensor design can be optimized, but the basic structure of the sensor like substrate thickness and width, electrode thickness didn't change. It will be explained in the following sections. Considering the measurable frequency range of the network analyzer in LMST and the proper working frequency range of SAW sensor in reference[37], working frequency of the SAW sensor in this work was decided in the range of 100 MHz to 200 MHz. And according to K. M. Mohibul Kabir's model [35], the initial electrode width and pitch length were decided. The pitch was initially set to $24 \mu\text{m}$ and electrode width was set to $6 \mu\text{m}$. Thus the resonant frequency of the SAW sensor can be calculated as 131 MHz with Equation (3).

Table 1 Model parameters in simulation.

Name	Value	Description
ws	1000 μm	Substrate width
ts	500 μm	Substrate thickness
we	6 μm	Electrode width
le	1500 μm	Electrode length
te	100 nm	Electrode thickness
rou	19300 kg/m^3	Electrode density
V0	1 V	Input voltage magnitude
vR	3158 m/s	SAW velocity
p	24 μm	pitch
f0	$vR/p=131.58$ MHz	Resonant frequency
ld	66 μm	Delayline length

According to [44], the mercury atoms diffuse only up to a 10 nm depth from the surface, which means only the top 10 nm gold layer would have a density change. Thus a 10 nm layer was built on top of the electrode. There were 30 IDTs (15 pairs) in each port. The width and thickness of the substrate are 1000 μm and 500 μm respectively.

Both input and output IDTs were divided into 2 groups, 1 group as terminal for input (terminal 1) or output signal (terminal 2) and the other group set as ground. A 1V static voltage was applied on terminal 1, and terminal 2 was set to 0 charge. Two free substrate edges were set as low reflection boundaries to eliminate the interference of reflection wave. The simulation was carried out in frequency domain and the transmission coefficient S_{21} was calculated. The S_{21} shows the frequency response of the SAW sensor, it can be calculated by Equation (9).

$$S_{21} = 20 \log_{10} \left(\frac{V_2}{V_1} \right) \quad (9)$$

V_1, V_2 is the voltage on terminal 1 and terminal 2, respectively.

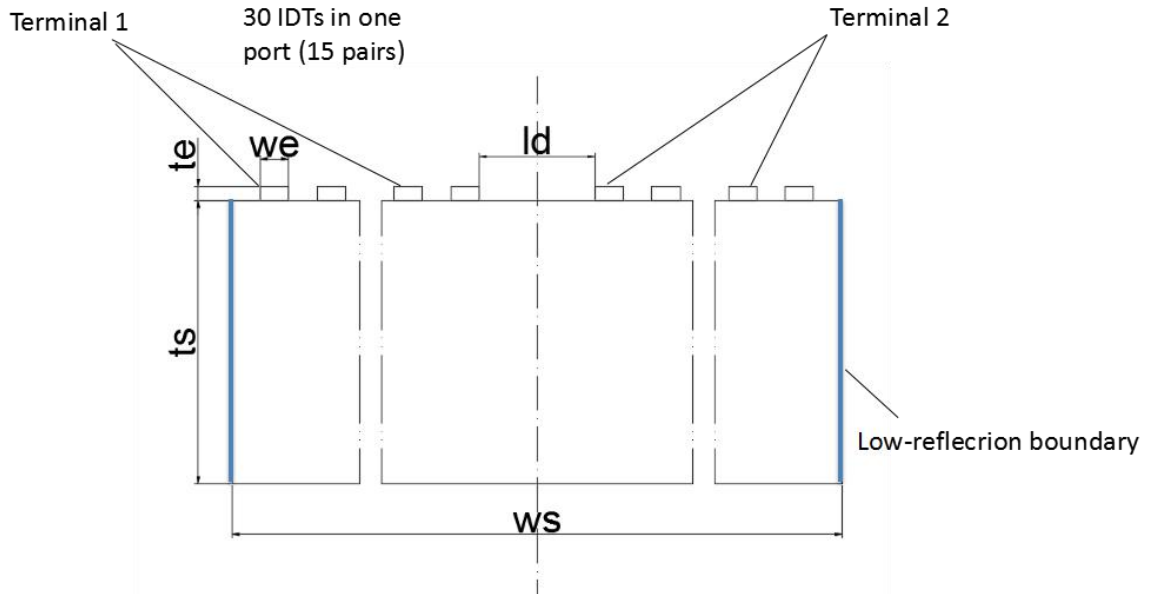


Figure 22 Schematic of the SAW sensor model. All electrodes are gold and substrate is ST-cut quartz.

The substrate material was chosen as ST-cut quartz because of its good temperature stability and low electro-mechanical coefficient that can minimize the acoustoelectric perturbation. However there's no ST-cut quartz in COMSOL's material database, so the Y-cut quartz, which is very similar to ST-cut quartz (the ST-cut quartz is also known as 42.75° rotated Y-cut quartz) was used in the simulation.

The characteristics of the two materials are shown in Table 2. It can be observed they are almost identical while the Y-cut quartz has a larger temperature coefficient. But temperature was not introduced into the simulation, so it has not impact on the results.

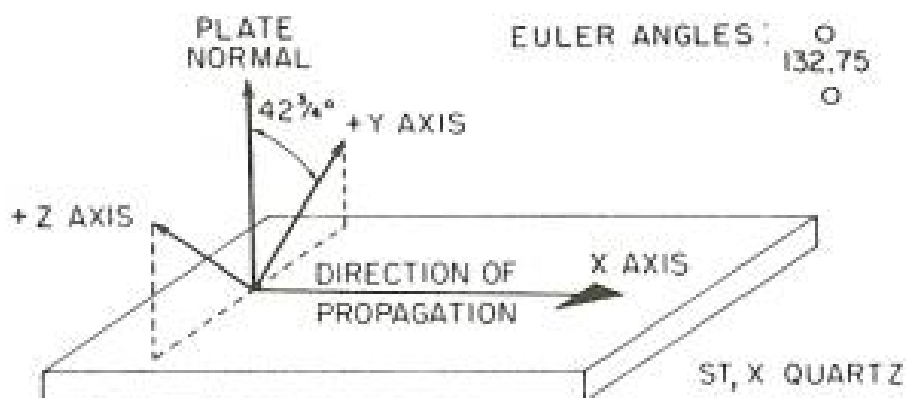


Figure 23 Orientation of ST-cut quartz [45]

Table 2 Characteristics of ST-cut quartz and Y cut quartz [46]

Material	Velocity (m/s)	Temperature coefficient (ppm/°C)	Coupling Coefficient (%)
Y cut quartz	3159	-24	0
ST cut quartz	3159	0	0.16

To ensure the accuracy of the simulation while reducing the calculation workload, custom mesh was applied. The surface acoustic wave mainly propagates through the surface, plus the electrodes are placed on the substrate surface which means most of the piezoelectric effect occurs near the surface. So the mesh close to the surface should be finer compare to other part of the model.

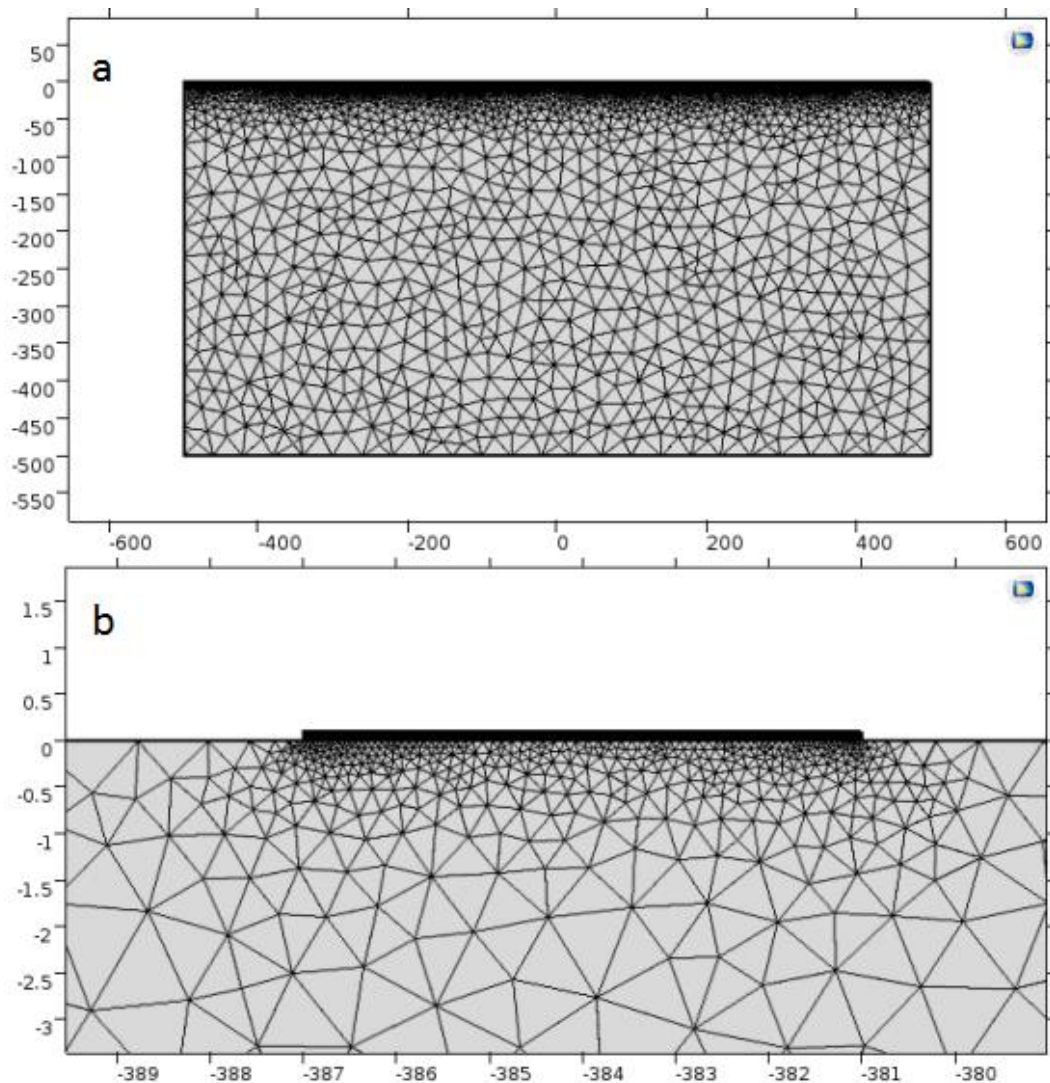


Figure 24 (a) Custom mesh built in FEM model (b) Mesh near an electrode. Areas closer to the electrode got finer mesh elements.

Specific numbers of mesh elements were manually distributed to the delay line between two IDT ports and the blank areas at both ends of the substrate surface to keep the mesh size at the same level with areas where electrodes were placed. Though the delay line length is shorter than the blank area, the surface acoustic wave must go through the delay line to reach terminal 2. Consequently, it needs more mesh elements

than the blank areas to ensure the accurate presence of the surface acoustic wave. The delay line and blank areas were all distributed 50 mesh elements. After custom mesh, there are at least 8 elements in each wavelength near the surface area. The closer to the bottom the coarser the mesh element is. The total element number is 297465. The built mesh is shown in Figure 24 (a), (b).

Different frequency ranges and different frequency steps were used according to different goal of simulation. This will be discussed in the following section.

3.2 Optimizing The SAW Sensor Design Through FEM Simulation

3.2.1 Resonance frequency and sensor characterization

After the model was built, a wide range frequency domain simulation was done as the first step to obtain the resonance frequency in the simulation model. The initial model with 24 μm pitch and 6 μm electrode width and a later version with 20 μm pitch and 5 μm electrode width were tested. Theoretical resonance frequencies of the two SAW sensor design can be calculated with Equation (3), as 131 MHz for 24 μm pitch design and 157.9 MHz for 20 μm pitch design. According to the theoretical calculation 2 wide range simulations were done. The frequency step applied was 0.1 MHz in both case but the frequency ranges were different due to different shape of the frequency curves. The simulation results are shown in Figure 25 (a) and (b). The simulated results show a 138.6 MHz resonance frequency for 24 μm pitch design and a 169 MHz resonance frequency

for 20 μm pitch design. The errors are 5.8% and 7% respectively.

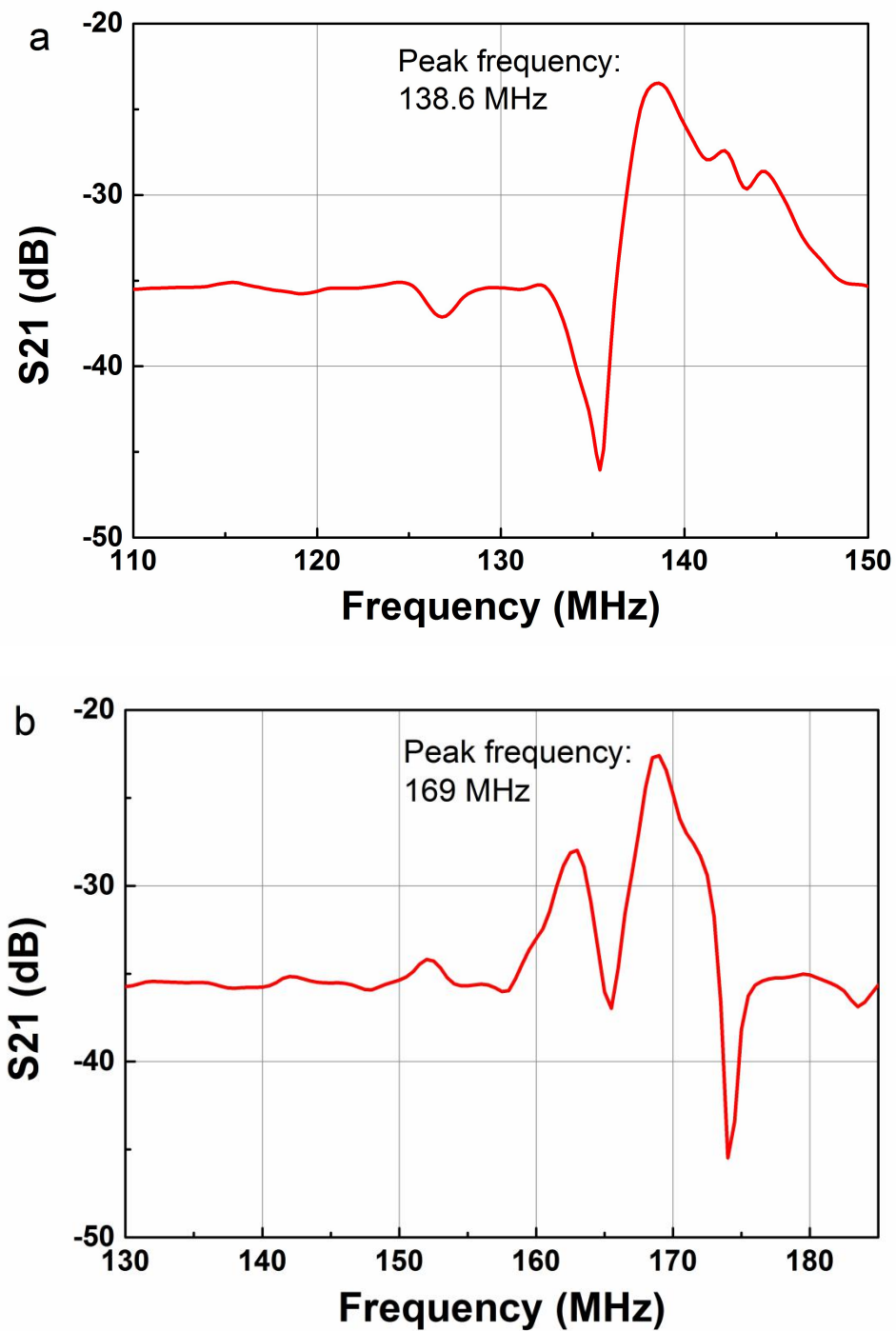
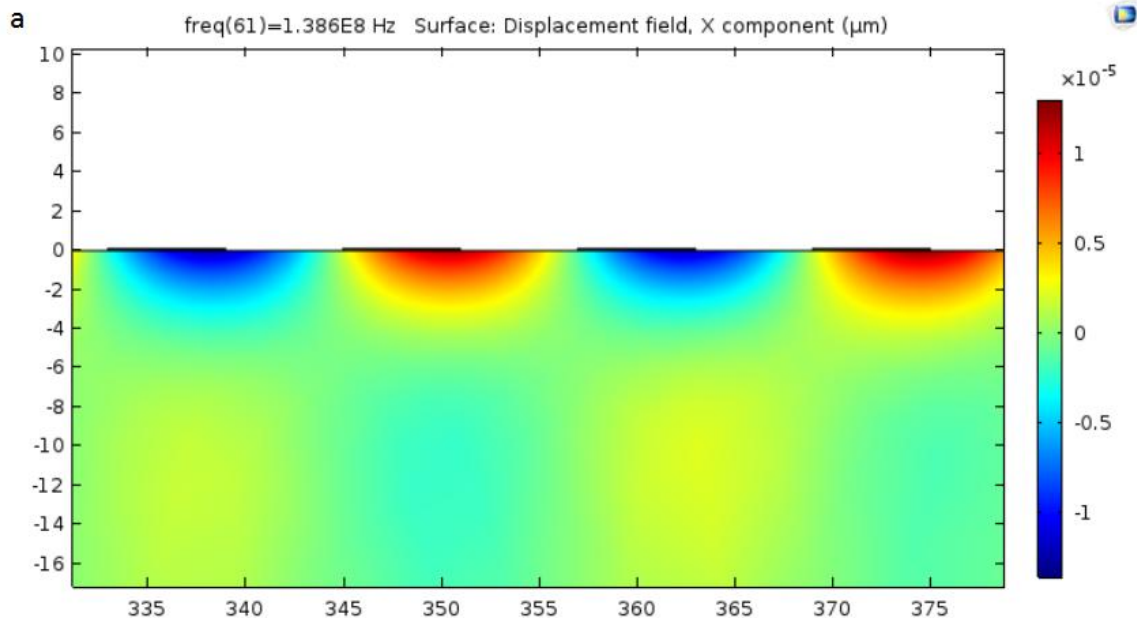


Figure 25 Simulation result of resonant frequencies for sensor with (a) 24 μm pitch, 6 μm electrode width (b) 20 μm pitch, 5 μm electrode width.

The surface deformation at the simulated resonance frequency was obtained in COMSOL Multiphysics. It can be observed that the resonant pattern shown in Figure 26 was consistent with the characteristic of Rayleigh Wave shown in Figure 18. The wave only propagates in the near surface area and the adjacent areas where electrodes set with voltage and ground had opposite displacement. It is worth noticed that the simulated frequency response result of sensor with 20 μm pitch, 5 μm electrode width has two peaks, both with a pattern that is consistent with Rayleigh wave except the smaller peak has smaller displacement magnitude. This is probably caused by the inaccuracy of the simulation model and needs to be verified in experiment.



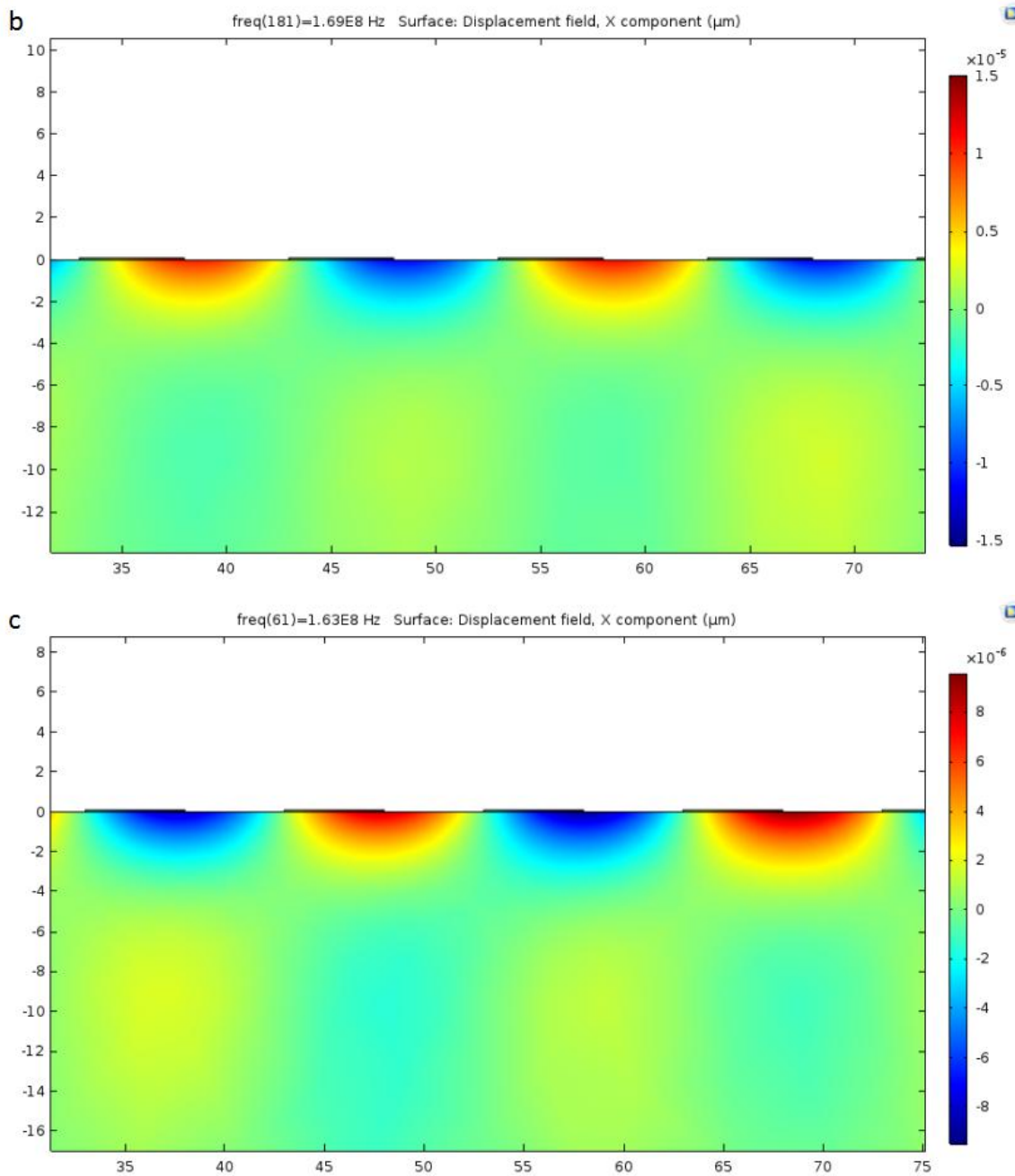


Figure 26 The displacement field of sensor with (a) 24 μm pitch, 6 μm electrode width at 138.6MHz, (b) 20 μm pitch, 5 μm electrode width at 169MHz, (c) 20 μm pitch, 5 μm electrode width at 163 MHz

Then the sensor characteristics were studied. It was mentioned in the previous section that the sensing element for the SAW sensor in this work is gold electrodes and

the adsorption of mercury vapor will lead to a density change of gold electrodes. The mercury absorption process forms mercury monolayers on surface of gold electrodes, causing density and thickness increase at the same time. The thickness increase is very small (6 nm for 20 monolayers)[35] so it was ignored in this model, making density change the only reason for the frequency shift of SAW sensor.

The mercury monolayer formed on the gold surface is not continuous layer, making it hard to study the sensor response during the adsorption process. Thus for the purpose of calculation and simulation, the concept of nominal monolayer is applied. A nominal monolayer can be defined as a layer of Hg atoms having same surface atom density as gold surface[39]. One nominal mercury monolayer is equivalent to 469 ng/cm² [47].

Therefore for the electrode design with length L=1500 μm and width W=6 μm, mass of one mercury nominal monolayer can be calculated as:

$$m_0 = L \times W \times 469 \text{ ng/cm}^2 = 0.04221 \text{ ng} \quad (10)$$

Since the mercury diffuse only up to a 10 nm depth from the surface, the density change of the 10 nm gold layer is:

$$\Delta\rho_0 = m_0/V = m_0/(W \times L \times 10 \text{ nm}) = 469 \text{ kg/m}^3 \quad (11)$$

When 20 nominal monolayers are formed, the gold surface reaches saturation, therefore, the density change of the gold film approaches a maximum and stops[35]. The frequency responses when 0, 5, 10, 15, 20 mercury monolayers are formed were

simulated. Result data was exported and processed in Matlab. It can be observed from the result in Figure 27 that the resonance frequency decreases with the density increase of the electrode top layer. Figure 28 shows the relationship between the magnitude of frequency shift and number of monolayers. The magnitude of frequency shift is approximately linearly proportional to the number of monolayers, which means frequency shift is proportional to density increase of top electrode layer. This result is consistent with Equation (8). Thus the validation of this FEM model was confirmed. The error in resonance frequency was most likely caused by the 2D simplified model and the different substrate material used. Next step is to optimize the sensor design for better performance.

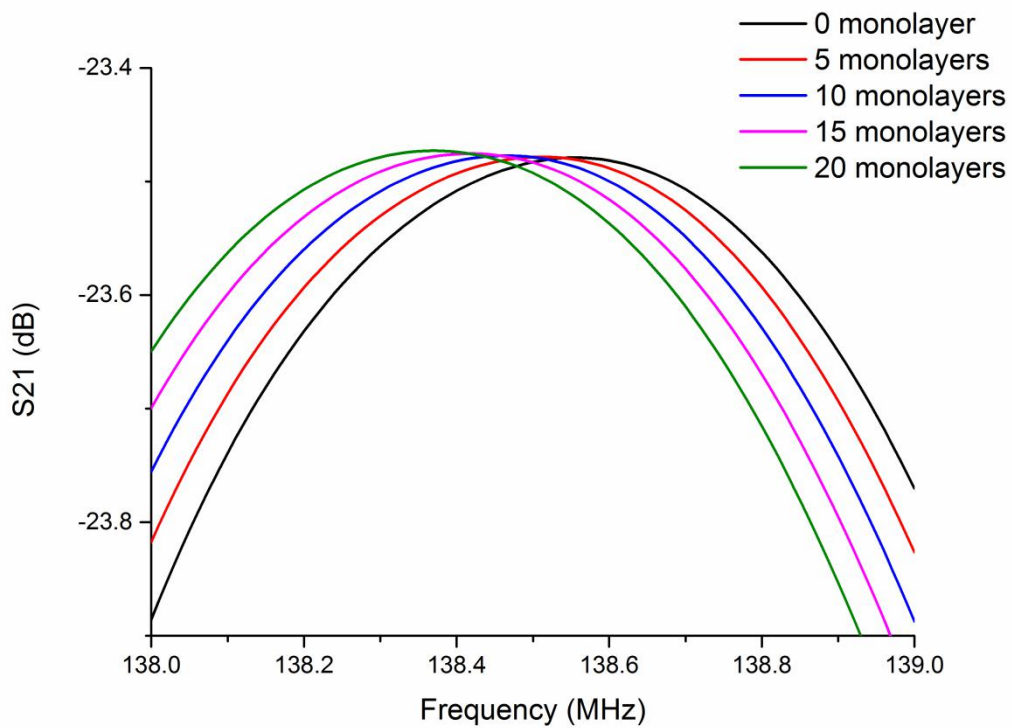


Figure 27 Simulated negative frequency shift due to mercury absorption

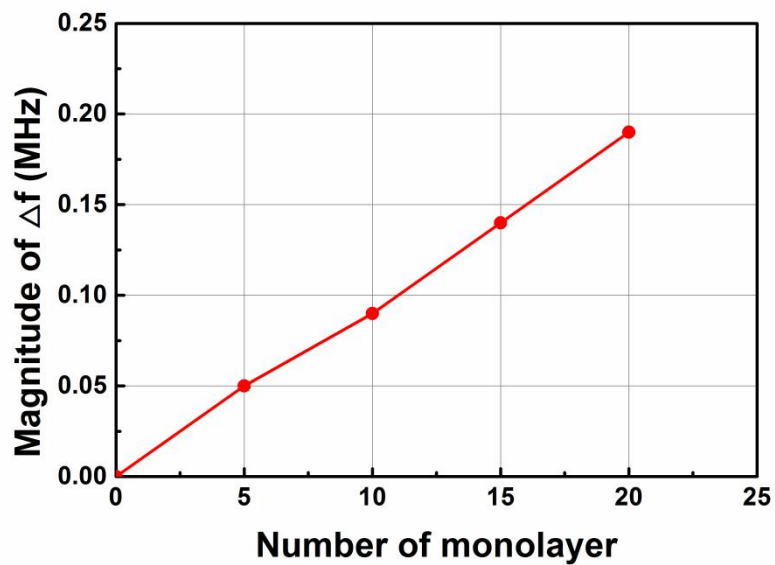


Figure 28 Relationship between number of monolayers and magnitude of frequency shift, sensor with 24 μm pitch, 6 μm electrode width.

3.2.2 Effect of electrode width and pitch

The characteristics of a sensor include many aspects, the sensitivity and the response time was studied in the simulation model. First, the sensitivity was studied for different design. Among all parameters that can be changed the electrode width was studied first because the electrode performs as the sensing element in this design, it will have direct influence on the wave generation. The electrode width is changed while keeping the pitch constant. The frequency shift of sensors with 24 μm pitch and 5 μm , 6 μm , 7 μm and 8 μm electrodes were simulated. The results are shown in Figure 29. The frequency shift of different sensor design are all approximately linearly proportional to the number of monolayers which is consistent with theoretical Equation. It can be observed that with the same monolayer number, the frequency shift increases with electrode width except for sensor with 8 μm electrode width. Its frequency shift magnitude is smaller than sensor with 7 μm electrode width but larger than sensor with 6 μm electrode width.

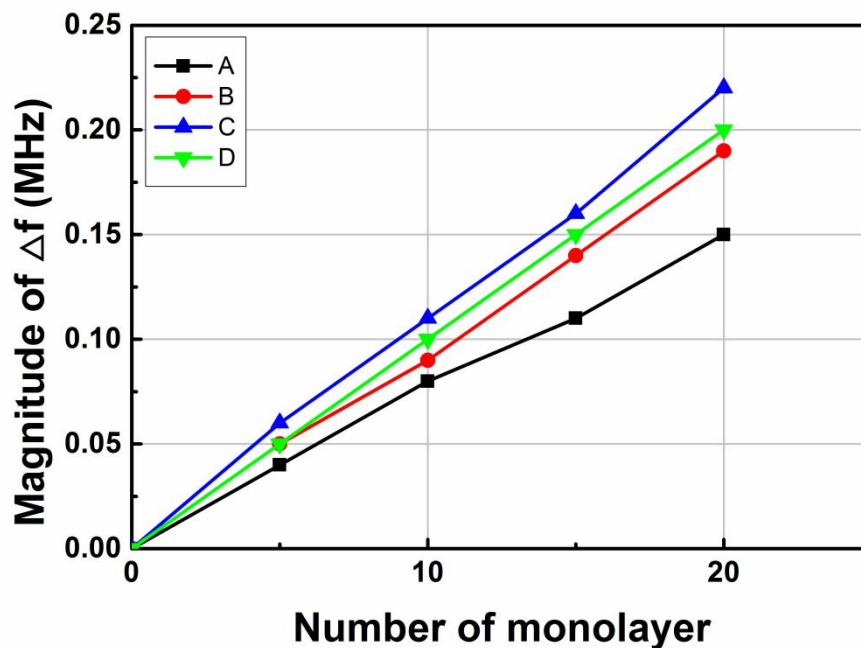


Figure 29 Frequency shift of sensor with 24 μm pitch (A) 5 μm electrode width (B) 6 μm electrode width (C) 7 μm electrode width (D) 8 μm electrode width

Then the influence of the pitch was studied. The pitch was decreased to 20 μm , the frequency response of sensors with 5 μm , 6 μm and 7 μm electrode width were simulated. The result is shown in Figure 30. The same tendency occurs in this group of result, the absolute frequency shift increases with electrode width except for sensor with 7 μm electrode width. From the two groups simulation results it can be observed that within certain range the larger electrode width can increase the frequency shift, which means the sensitivity of the sensor is increased. However if the electrode width exceeds certain range, the sensitivity will decrease.

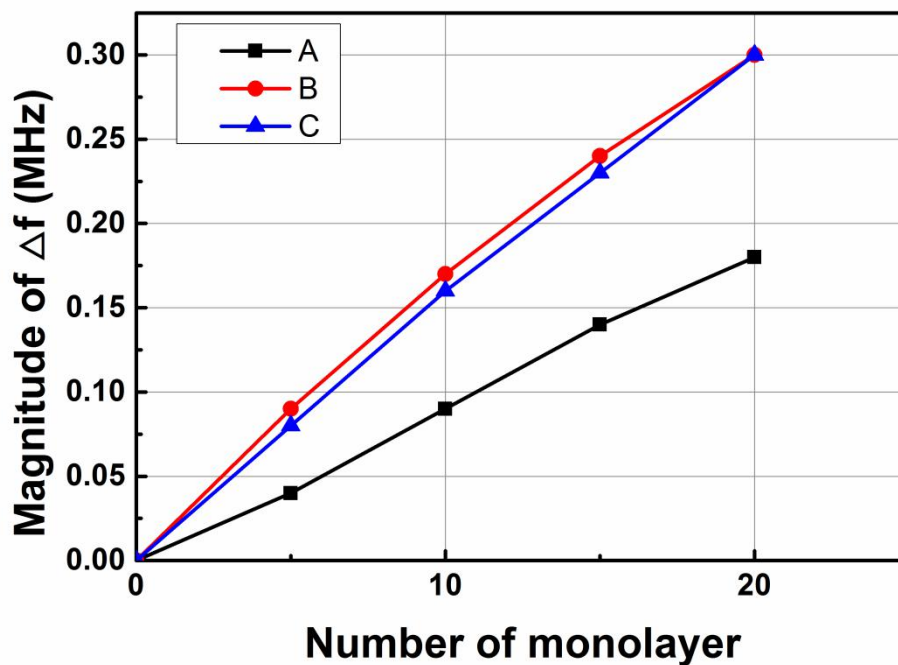


Figure 30 Frequency shift of sensor with 20 μm pitch (A) 5 μm electrode width (B) 6 μm electrode width (C) 7 μm electrode width

The comparison between sensors with same electrode width but different pitch is shown in Figure 31. It's clear from the results that sensors with 20 μm pitch have larger frequency shift when the same amount of monolayers are formed on the gold film. It can be observed from these results that under the same condition, smaller pitch can result in better sensitivity.

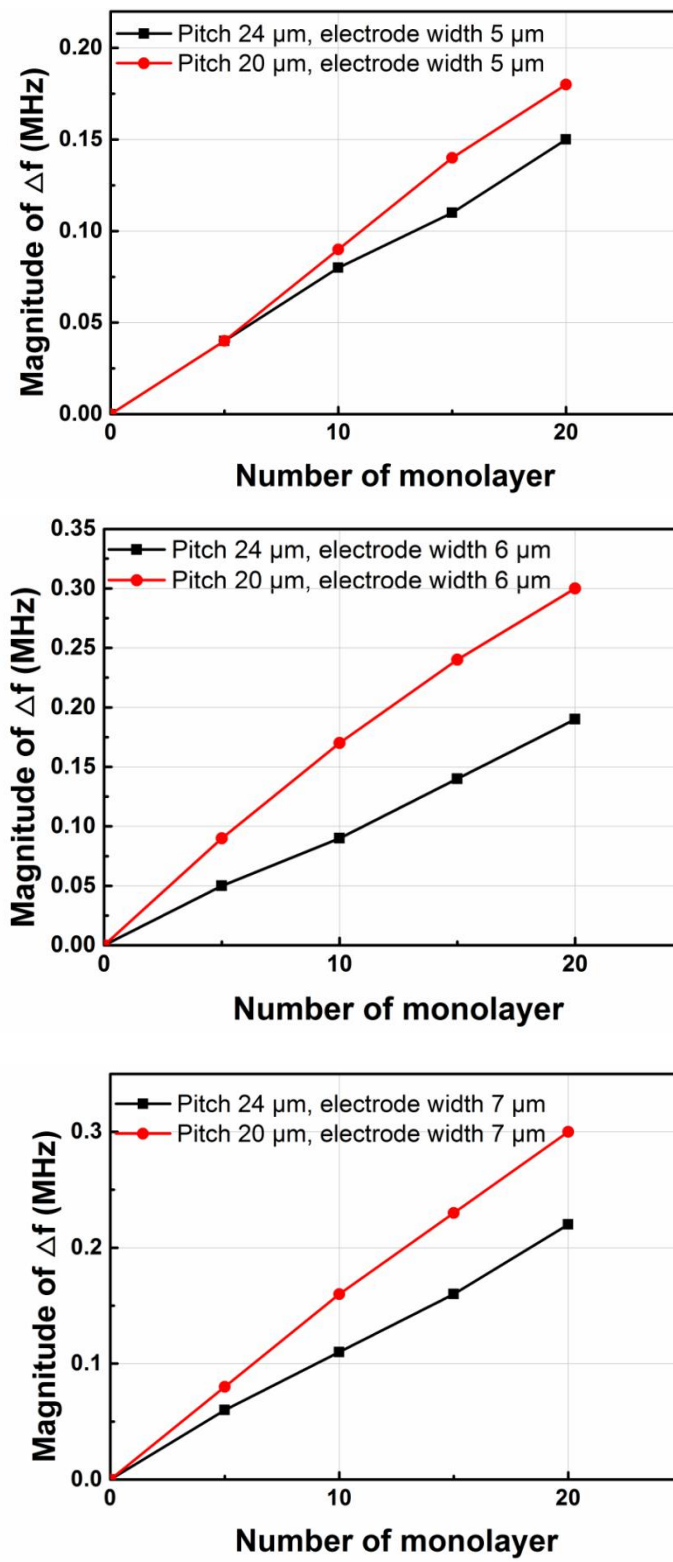


Figure 31 Comparison between sensors with same electrode width but different pitch

Then the response time was studied. The times needed to form different monolayers were calculated. The sticking coefficient of mercury on gold is approximately unity[48], thus it can be treated as all mercury atoms would be absorbed when coming into contact with gold electrodes. The mercury vapor concentration needs to be detected is $C = 1 \mu\text{g}/\text{m}^3$, the flow rate of mercury vapor generated by the mercury generator in our lab is adjustable, the maximum flow rate on the instruction, $R_f = 2\text{L}/\text{min}$ is used for calculation. Assuming the sticking coefficient doesn't change, and all the mercury generated will be taken into the testing chamber and absorbed by the gold electrode until the surface reaches saturation, which means when 20 monolayers are formed[35]. The mass flow rate of mercury goes into the chamber can be calculated as:

$$M_f = C \times R_f = 0.002 \mu\text{g}/\text{min} \quad (12)$$

Mass of one monolayer mercury on one $6 \mu\text{m}$ wide electrode was calculated in the previous section as $m_0 = 0.04221 \text{ ng}$. There are total 60 electrodes on the model so the time to form one mercury monolayer can be calculated as:

$$t_{1-6} = m_0 / M_f = 1.2663 \text{ min} \quad (13)$$

It should be noted that sensor with different surface areas has different time to form one mercury monolayer. In a similar way the times can be calculated.

The results for response time are shown in Figure 32 and Figure 33. Since the different surface areas lead to different time to form mercury monolayers, the results are

very different from sensitivity results. 0.15 MHz frequency shift was set as the required response. For the sensors with 24 μm pitch, it can be observed from the results in Figure 32 that though sensor with 7 μm electrode width has a better sensitivity, it took a little bit longer time to reach 0.15 MHz frequency shift. The sensor designs with 5 μm and 6 μm electrode width have worse sensitivities but they can reach the required frequency shift even faster than the sensor with 7 μm electrode width. This fact leads to similar response time. Before reach 20 monolayers, these three sensors perform almost the same. But the sensor with 8 μm electrode width didn't perform well as its response time is much longer compare to the other designs.

Results are similar for sensors with 20 μm pitch. However, among this group the sensor with 6 μm electrode width has a clear advantage to the other two. It has good sensitivity with good response time.

It also should be noted that the time calculation was based on several assumptions. In practical situations the sticking coefficient will change with the adsorption of mercury and it's not realistic for the gold film to adsorb all mercury atom taken into the test chamber. These assumptions were made in this part in order to simplify the model. It is difficult to analyze the actual mercury distribution in the test chamber and mimic the actual adsorption process with changing sticking coefficient. This simulation is only meant to study how the design can influence the response time rather than have the

accurate representation of sensor response time. And the all the simulation results should be verified in experiments.

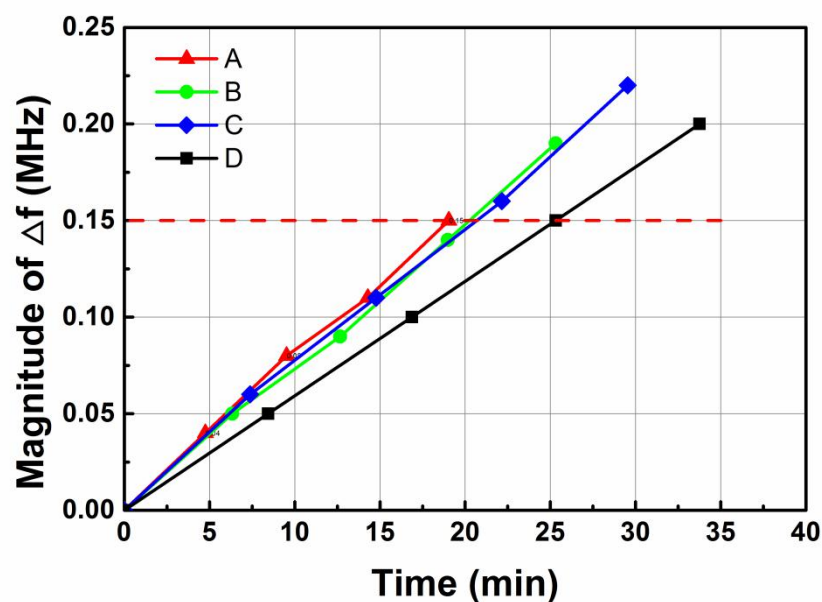


Figure 32 Simulated response time for sensors with 24 μm pitch (A)5 μm electrode width (B)6 μm electrode width (C)7 μm electrode width (D)8 μm electrode width

From these results sensor with 20 μm pitch, 6 μm electrode width perform the best in its group. For the 24 μm pitch group, sensors with 5 μm , 6 μm and 7 μm electrode width perform very similar but considering the sensor with 7 μm electrode width take longer time to reach 20 monolayers and has a better sensitivity it was a better choice. The comparison of these two sensors is shown in Figure 34. Clearly from the result sensor with 20 μm pitch and 6 μm electrode width have a big advantage over the other one both in sensitivity and response time.

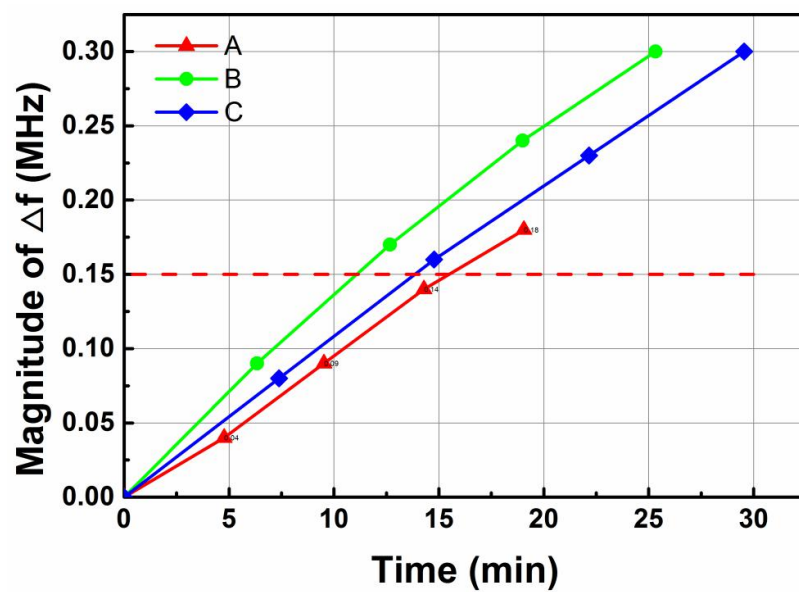


Figure 33 Simulated response time for sensors with 20 μm pitch (A) 5 μm electrode width (B) 6 μm electrode width (C) 7 μm electrode width

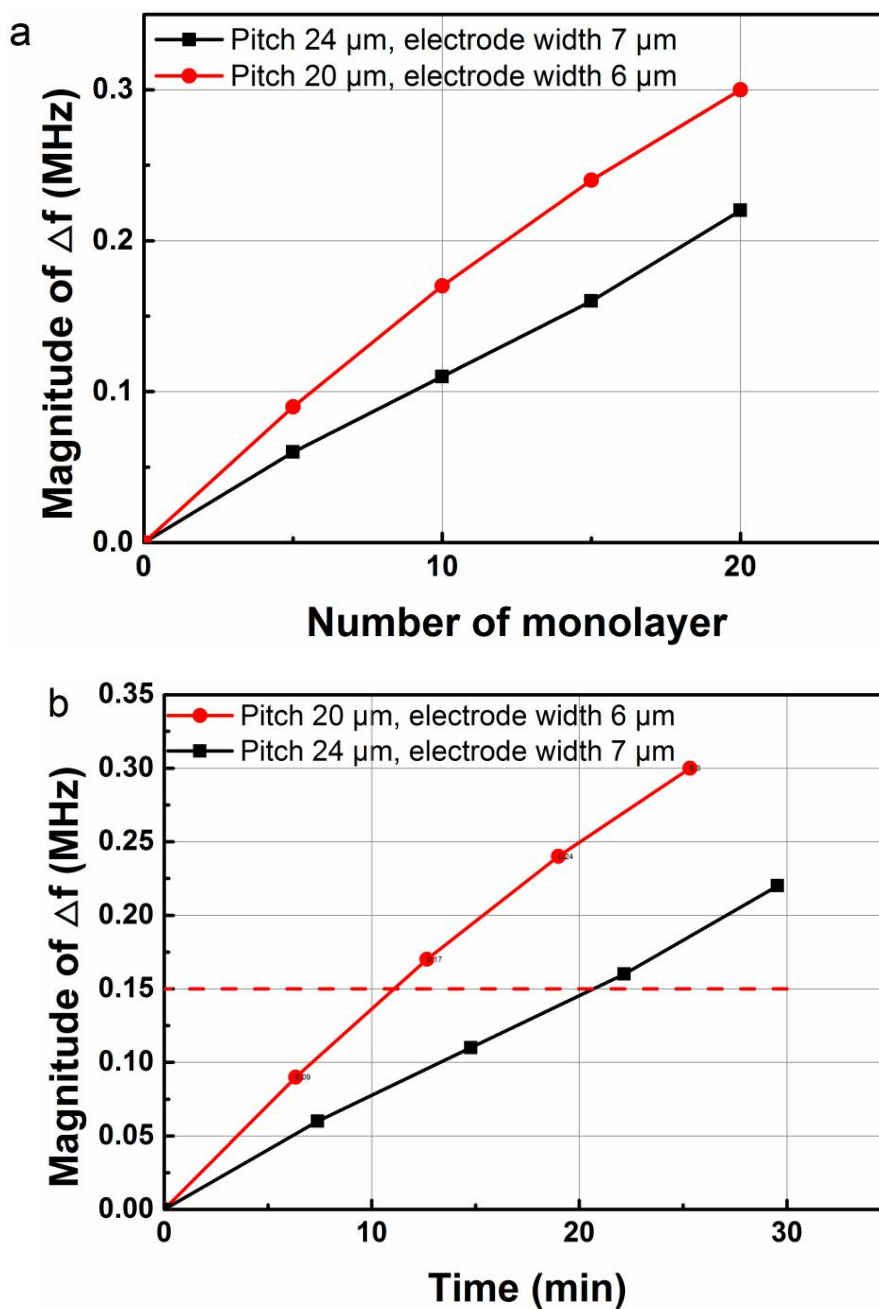


Figure 34 Comparison of the response of sensor with 24 μm pitch, 7 μm electrode width and 20 μm pitch, 6 μm electrode width (a) sensitivity, (b) response time.

The mechanism behind these results is unclear for now. But it can be observed that

the similarity of larger electrode width and smaller pitch is the gaps between electrodes are decreased. With the same potential difference, the shorter distance between two electrodes will result in a stronger electric field intensity E . According to piezoelectric constitutive Equation (1) the piezoelectric effect is the coupling between electric power to mechanical power[37] and also according to reference [37] the change of SAW velocity is fundamentally related to the change of the wave energy density. Thus it is hypothesized that the change in electric field results in the change of converted mechanical energy, which influenced the wave energy density and SAW velocity. It also should be noticed that these are all simulation results, still need to be verified in experiments.

3.2.3 Effect of delay line lengths

The influence of delay line length on the sensor was studied follow the pitch and electrode width. The sensor design with 20 μm pitch and 6 μm electrode width was used. The delay line length was reduced to 46 μm and increased to 86 μm and frequency shifts under the condition of a same number of monolayers formed on the gold surface were simulated. The result is shown in Figure 35. The result seems contradictory. Both increased delay line and decrease delay line perform worse than the original design.

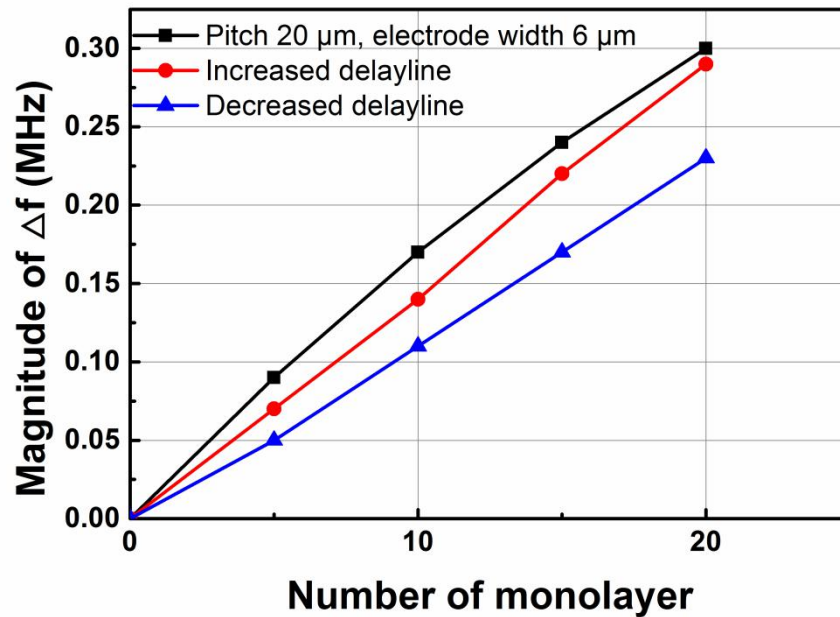


Figure 35 Simulated sensitivity of sensor with 20 μm pitch 6 μm electrode width with different delay line length.

As for the effect of the delay line length, for the sensor design in this work, delay line doesn't perform as the sensing element as in traditional designs. The length of the delay line may have an influence on the time delay of output signal because the travel distance of the signal changes, but it should not have influence on the sensitivity of the sensor according to the perturbation theory that Equation (4)[42] expressed.

The change of the sensitivity is probably because of the change of delay line length caused the change of mesh. Certain number of mesh elements was set to the delay line area, when the delay line length changes the number keep unchanged, so the mesh size has to change. This would influence the entire mesh and may cause the change of sensitivity. And the reason may also be the change of delay line length caused the change

of electrodes location, which caused the sensitivity difference. No conclusion can be obtained from this simulation and the effect of delay line length still need to be verified in experiment.

3.3 Summary of FEM Simulation And Design of SAW Sensor

There are a few preliminary results we can have from the simulation work. First, under the condition of same pitch and same number of monolayers are formed sensor with larger electrode width can have better sensitivity but if the electrode width exceeds certain extent, the sensitivity will start decreasing. Second, with same electrode width and same number of monolayers formed the smaller pitch results in better sensitivity. Third, the response time of different sensors could be similar.

According to the simulation results, the desired SAW sensor pitch and electrode width were optimized to 20 μm and 6 μm , respectively. The other design parameters were decided refer to [37]. The design parameters are shown in Table 3.

Table 3 Design parameters of SAW sensor

Substrate width	6 mm
Substrate length	14 mm
Electrode width	6 μm
Electrode length	1500 μm
Electrode thickness	100 nm
pitch	20 μm
Delayline length	1400 μm
Pairs of IDT in each port	200

CHAPTER FOUR: DEVICE FABRICATION AND TEST

4.1 SAW Sensor Fabrication

4.1.1 General steps of SAW sensor fabrication

Since the substrate material of SAW sensor was chosen as ST-cut quartz, 4-inch ST-cut quartz wafer was used in the fabrication process. The fabrication flow chart is shown in Figure 36.

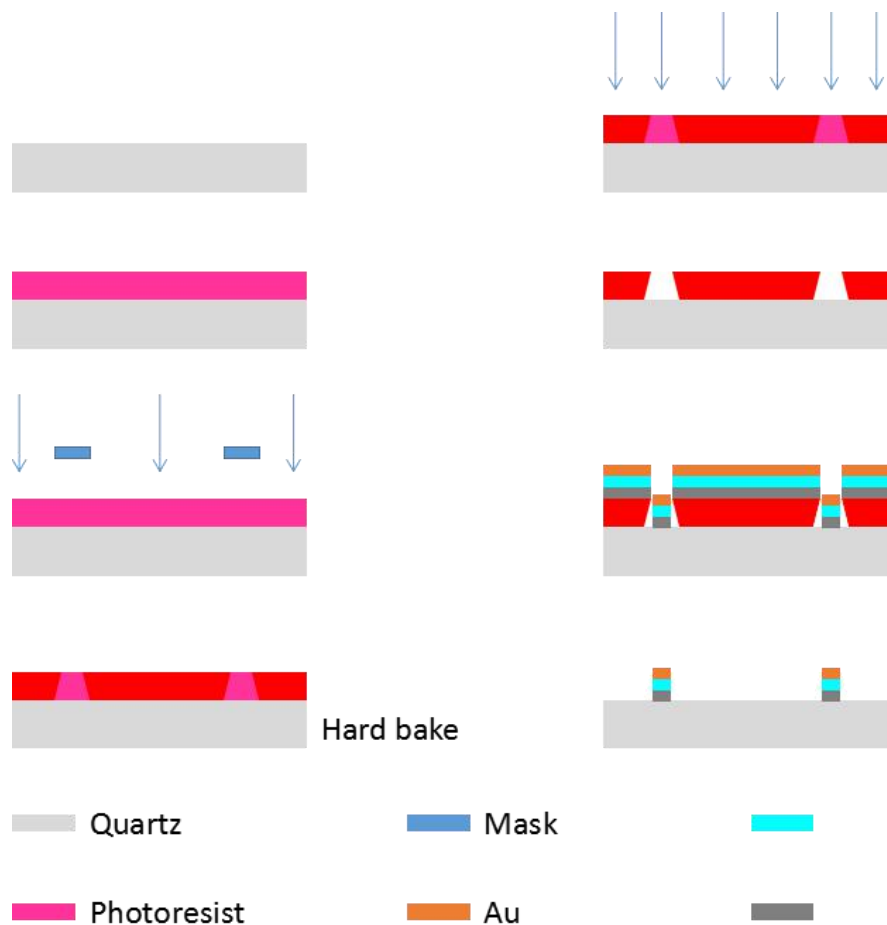


Figure 36 The fabrication process of the sensor.

First, the wafer is cleaned, then spin coated with photoresist for subsequent

photolithography. For the purpose of metal deposition and lift-off, an image reversal process is needed to create an undercut profile as shown in Figure 36. After the lithography, metal was deposited onto the wafer. The following lift-off process removes the photoresist, only leaving the metal electrodes on the substrate. Each fabrication step will be discussed in details in the following sections.

4.1.2 Cleaning and photoresist coating

The ST-cut quartz wafer was cleaned with piranha solution (H_2SO_4 : H_2O_2 3:1 in volume) for 10 min to clean off any organic residuals on the surface and dried on 110 °C hotplate for 2 minutes. To increase the adhesion of photoresist, first the quartz wafer was spin coated with a layer of HMDS at 4000 rpm for 45s. The spinning of the HMDS includes a 5 second spread at 500 rpm, a 45 seconds spin at 4000 rpm and a 5 second slow down at 500 rpm. For image reversal process, a layer of photoresist AZ 5214E was coated at 4000 rpm for 45s. The spinning of the AZ 5214E also includes a 5 second spread at 500 rpm, a 45 seconds spin at 4000 rpm and a 5 second slow down at 500 rpm. Then the wafer was baked on a hotplate at 110 °C for 1 minute.

4.1.3 Exposure and development

After the wafer was coated with AZ 5214E photoresist and baked, it was ready for exposure. It was mentioned in the previous sections that an image reversal process was needed to create the special undercut profile for the lift-off after metal deposition. For the

lift-off process, the typical undercut profiles for different procedure are shown in Figure 37[49]. When using positive photoresist for deposition and lift-off, it will create a positive wall profile shown in Figure 37. The sidewalls of photoresist will also be coated with metals and create a continuous metal film[50]. To finish the lift-off process, ultrasonic cleaning with acetone is needed to remove the photoresist and metal on it. Thus the long, thin IDTs in our work may be torn apart when the other parts of the continuous film are removed if using positive photoresist for lift-off process.

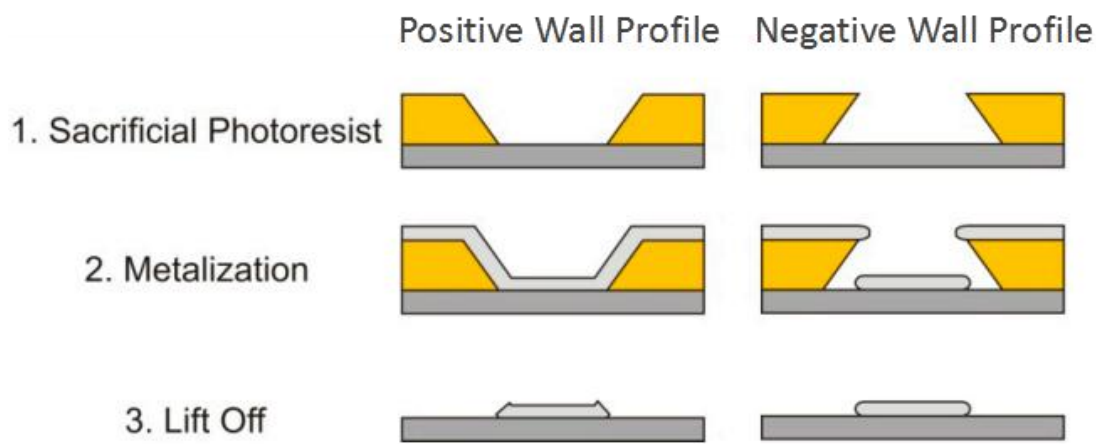


Figure 37 A schematic of lift-off process with positive and negative photoresists. [49]

A negative wall profile can be created when applying the image reversal process with AZ 5214E photoresist. A special crosslinking agent in AZ 5214 which activates above 110 °C in exposed areas together with exposed photoactive compound create an almost insoluble and light insensitive substance[51]. The other areas still have the characteristics of a normal positive photoresist. After the flood exposure and development, other areas

are developed away by developer while the crosslinked area remains. During this process due to the absorption of the photoactive compound, the light is attenuated when penetrating through the resist layer. At the top higher exposed areas is crosslinked to a higher degree than lower area with lower exposure. The final result is a negative wall profile.

The photolithography process was done with a Karl Suss MA6 mask aligner. The coated wafer was first exposed to 10 mJ/cm^2 UV light with mask for 3 seconds, then hard baked on hotplate at $120 \text{ }^\circ\text{C}$ for 1.5 minutes. After cool down the wafer was flood exposed with 10 mJ/cm^2 UV light for 60 seconds without mask. This step created the desired pattern for lift-off. The areas not needed were first exposed and baked to form the insoluble substance while areas where metals would be deposited to form IDTs still had the characteristics of positive photoresist.

The AZ 5214E photoresist was developed with AZ 400K developer. The wafer was developed for 15 seconds then rinsed with DI water for 1 minute. The areas where electrodes would be deposited were removed while other areas remained covered by photoresist.

During the fabrication process, a silicon wafer was used as dummy to verify the recipe. It was observed that the photoresist needed to be removed cannot be completely developed away when exposed for 4 seconds with mask and hard bake for 2 minutes

according to the recipe. The reasons of this could be the time of exposing with mask is too long, the covered areas were affected or the hard bake time is too long caused the property change in the photoresist. Therefore the exposure time was reduced to 3 seconds while the hard bake time kept unchanged. Same problem happened after this change. Then the hard bake time was reduced to 1 minute then after the development, the patterns were good and clear as shown in Figure 38.

After the exposure time and hard bake time were adjusted on the dummy silicon wafer the ST-cut quartz wafer was used in fabrication. However some of the small structure on quartz wafer was developed off after development shown in Figure 39. The structure was washed off means the formation of the insoluble substance in AZ 5214E was not ideal, but under the same condition the pattern on silicon wafer was much better indicated the process parameters used were generally correct, the reason was more likely the different characteristic of the substrate. Silicon has a much larger thermal conductivity(149 W/(m •k)[52]) than quartz (11.1 W/(m •k)[53]) so when they were hard baked for the same amount of time, more heat was transferred to the AZ 5214E photoresist on silicon wafer and improved the formation of the insoluble substance. The hard bake time was extended to 1.5 minutes for quartz and the structures were good after development (Figure 40). It is a noticeable fact for different substrate materials the fabrication technology can be different due to their characteristic. The fabrication

technology of SAW sensor was cleared up through this work, laid the foundation of future related works.

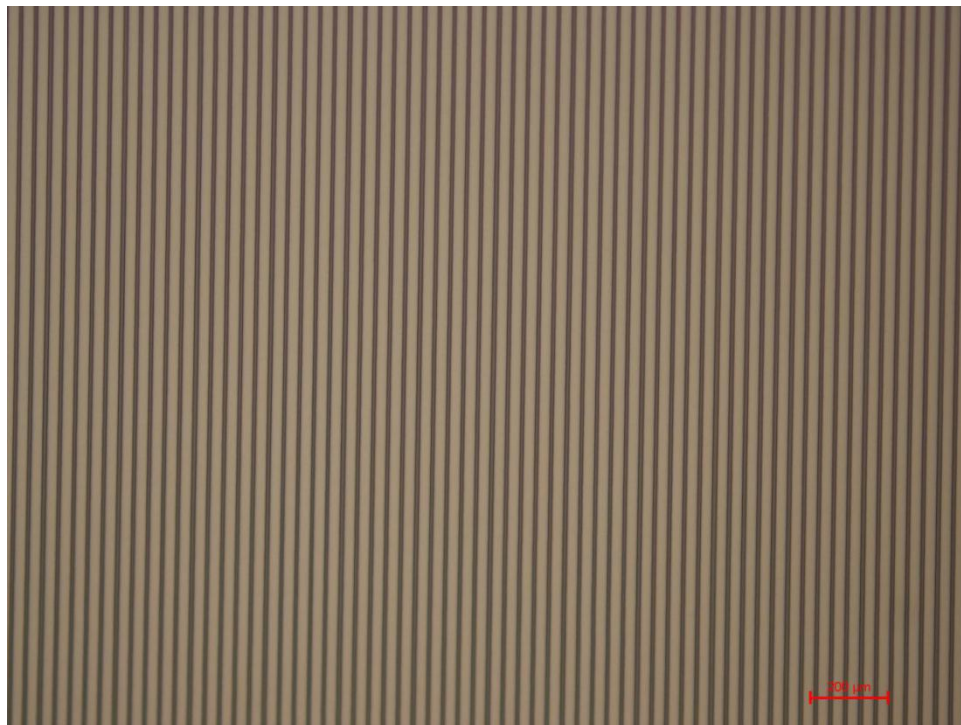


Figure 38 Microscope figure of IDT patterns on silicon wafer with 3 s exposure time and 1 min hard bake



Figure 39 Microscope figure of IDT patterns on ST-cut quartz wafer with 3 s exposure time and 1 min hard bake

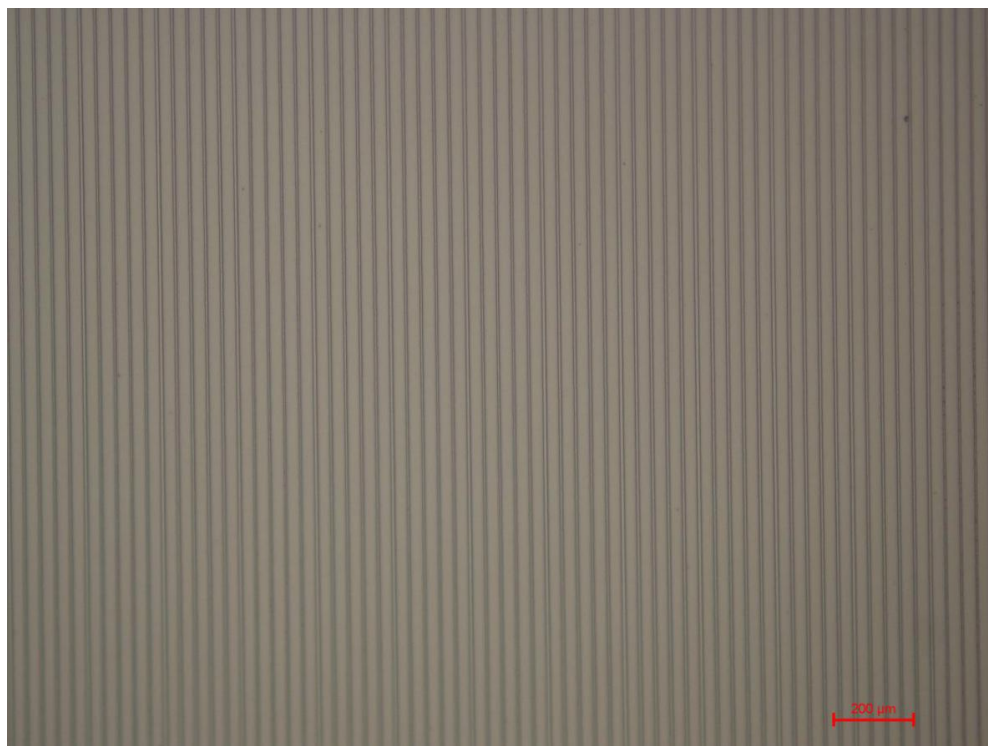


Figure 40 Microscope figure of IDT patterns on ST-cut quartz wafer with 3 s exposure time and 1.5 min hard bake

4.1.4 Metal deposition and lift-off

In this work, metals were deposited onto the substrate with a CHA Industries Solution System. A layer of 20 nm thick Ti and a layer of 30 nm thick Ni were deposited on the quartz substrate to serve as adhesion layer. A layer of 50 nm gold was deposited followed the Ti and Ni layer at the rate of 0.05 nm/s. The deposition process took around 1 hour included the time to change metals.

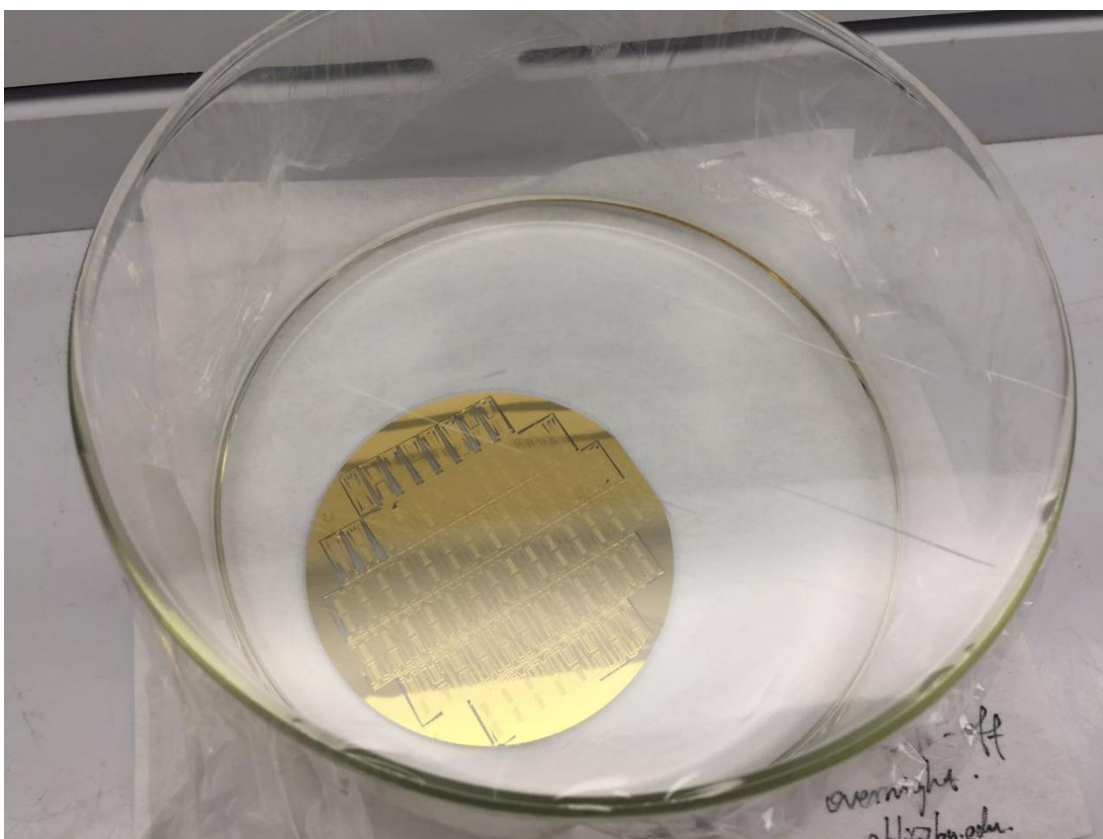


Figure 41 Sample during lift-off process

After the metal deposition, the unwanted metals on photoresist were removed by lift-off process. The sample was soaked in acetone overnight and then cleaned in an

ultrasonic cleaning machine with acetone. When the unwanted parts were removed, the desired SAW sensor structures were left on the sample.

4.1.5 Dicing saw cutting and printed circuit board (PCB) bonding

The sample was cut into single SAW sensor with a dicing saw. For quartz substrate cutting the cutting velocity was set to 3 mm/s. Before the cutting, the sample was spin coated with a layer of S1818 photoresist to protect the SAW sensor structures on it. The S1818 was spun at 3000 rpm for 40 seconds. The sensor needs to be cleaned with ultrasonic cleaning machine in acetone for 1 minute before use. Figure 42 shows the SAW sensor after cutting.

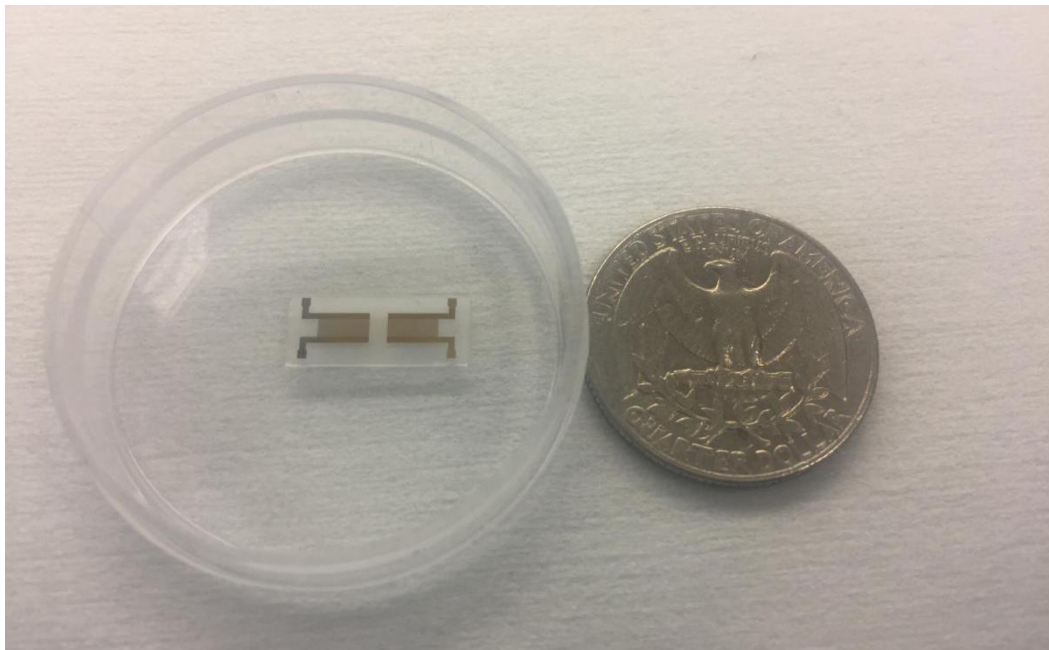


Figure 42 Fabricated SAW sensor

Designed copper clad board bonding was used for the convenience to connect the

sensor with connector and testing devices. The PCB was first covered with a layer of plastic film for layout printing and corrosion. The layout was designed with AutoCAD and printed on the plastic film using a laser printing machine. The plastic film on the unwanted areas was removed after laser printing. The PCB was etched in 40% H_2SO_4 and H_2O_2 solution for 10 minutes. After cutting 2 SMA connectors were welded to the PCB, and the SAW sensor was bonded on the PCB and connected with SMA connectors with silver epoxy adhesive.



Figure 43 Laser printing machine

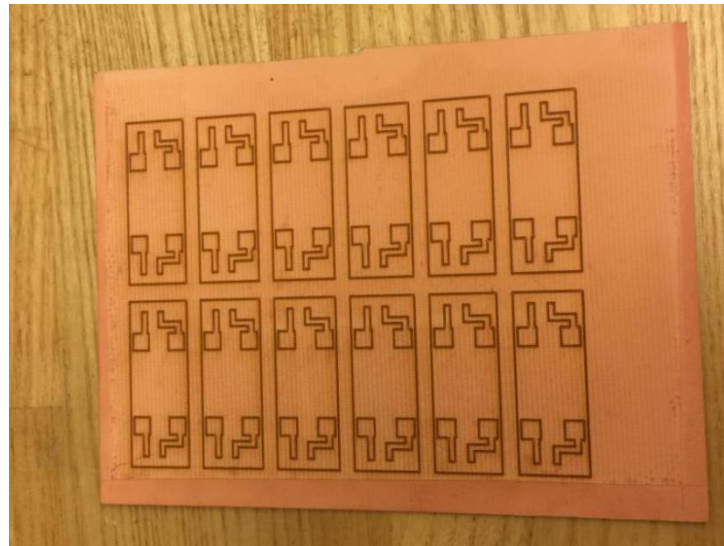


Figure 44 PCB after laser printing

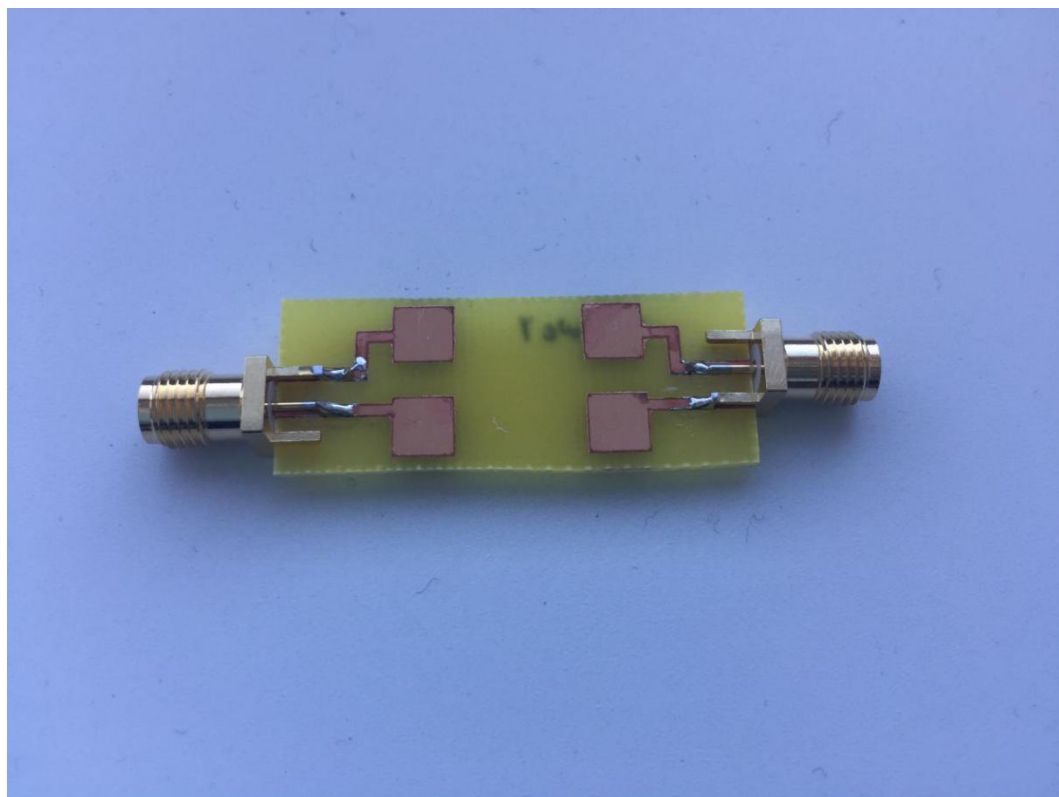


Figure 45 PCB with welded SMA connector

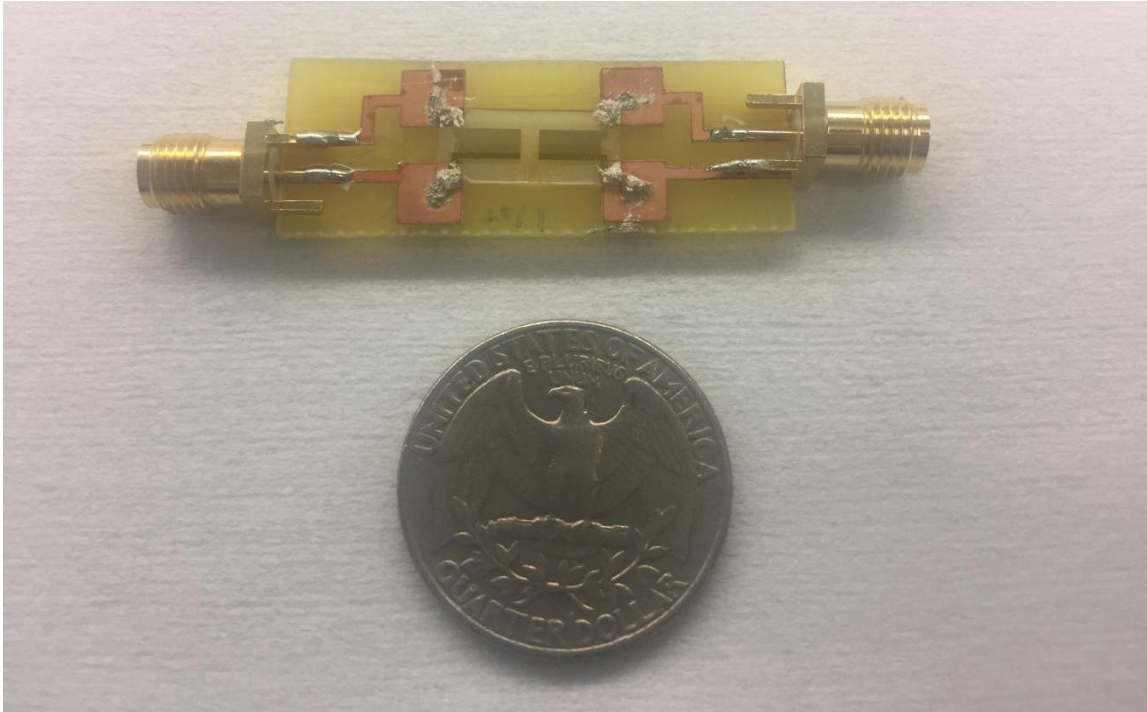


Figure 46 Sample SAW sensor

4.1.6 Fabrication summary

In this work, 3 designs of SAW sensor with 20 μm pitch/5 μm electrode width, 20 μm pitch/6 μm electrode width and 24 μm pitch/7 μm electrode width were fabricated. These designs were selected because sensor with 20 μm pitch 6 μm electrode width and 24 μm pitch 7 μm pitch perform best in their group in the simulation, and sensor with 20 μm pitch 5 μm was fabricated to verify SAW sensor electrode width's effect on its characteristic.

The two key structure parameters of fabricated sample sensor, pitch and electrode width were measured. The sensors with 20 μm pitch 5 μm electrode width had an

average pitch of 20.31 μm and an average electrode width of 5.825 μm . The sensor with 20 μm pitch 6 μm electrode width had an average pitch of 20.37 μm and an average electrode width of 6.93 μm . And the sensor with 24 μm pitch 7 μm electrode width had an average pitch of 24.51 μm and an average electrode width of 8.03 μm . All averages were calculated from 10 measured values. It can be observed from the results that the pitches of the fabricated sensor were close to the design, but the electrode width had quite large errors. The error even exceeds 1 μm which is the amount of length change in design. The larger electrode width with same pitch means the gap between electrodes were smaller, in other words the areas where the insoluble substance supposed to form were smaller than the design. This could be attributed to the insufficient expose time. Light attenuates when penetrates through the photoresist, with insufficient expose time some areas were not exposed thus the gaps were smaller. The large errors in electrode width will interfere the study of the effect of electrode width on sensor response, the fabrication still needs to be improved.

4.2 SAW Sensor Test And Mercury Sensing Experiment

4.2.1 Test setup

The test setup for mercury sensing consists of three major parts: 1. Computer control unit, 2. Mercury vapor generator and 3. Test chamber. The computer control unit is shown in Figure 47.

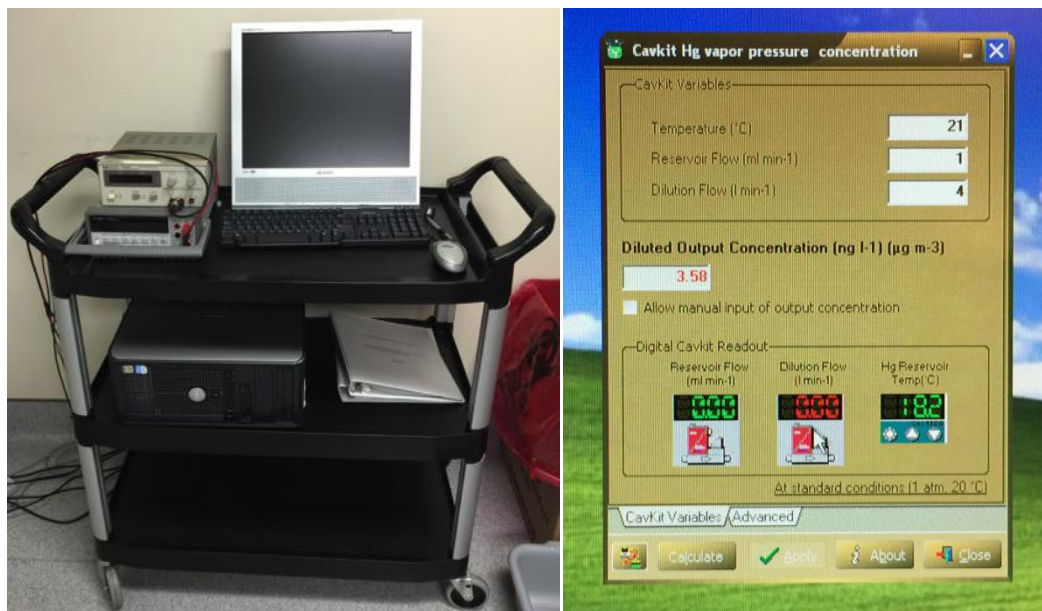


Figure 47 The computer control unit of the test setup.

A program running on the computer can control the temperature of the mercury reservoir (in °C), the flow of the reservoir (in ml/min) and the dilution flow (in l/min). By calculating the evaporation speed of mercury at certain temperature and also considering both the reservoir flow and dilution flow, the program can get a diluted output concentration (ng/l, or $\mu\text{g}/\text{m}^3$).

The mercury vapor is generated by a PSA 10.536L low-level mercury calibration system. A Certain concentration of mercury vapor is produced by the principle of diluting the known output of a mercury permeation tube. Two mass flow controllers are used in the system to maintain accurate flow rates. The permeation rate of the permeation tube is kept constant with an oven arrangement. Figure 49 shows a schematic of the mercury generating system. Air controlled by a mass flow controller (MFC1) pass

through the permeation tube chamber at a low flow rate of 0-20 ml/min. The mercury vapor flow then is mixed into a dilution air stream supplied by the second mass flow controller (MFC2) to dilute the Hg vapor into the required concentration range.



Figure 48 PSA 10.536L Hg generator

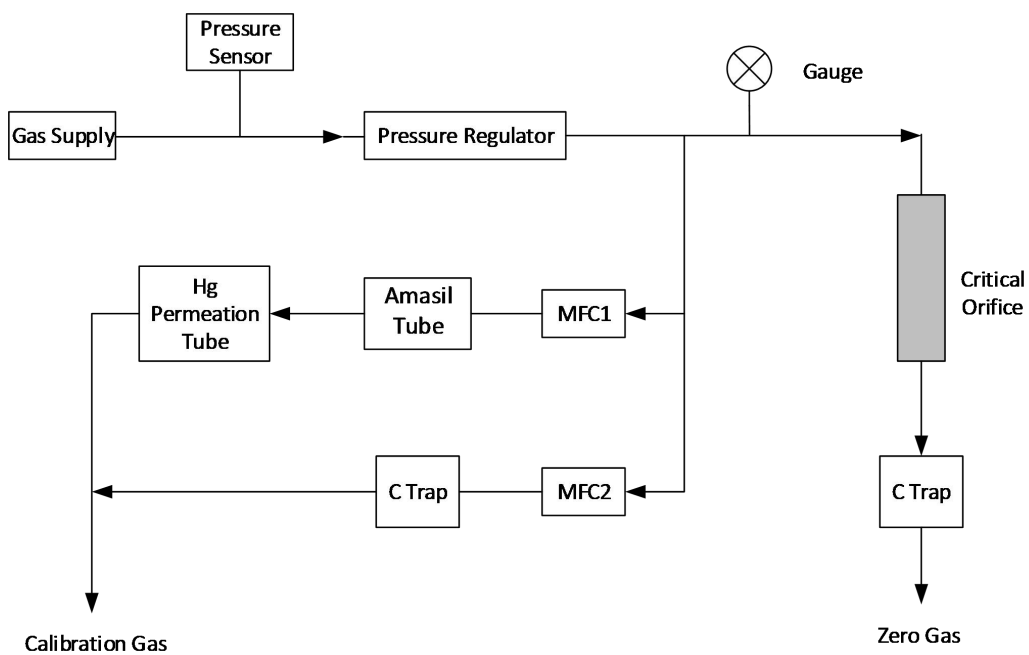


Figure 49 Schematic Diagram of Hg generating system

Figure 50 shows the structure of the test chamber. It is made of mercury absorption-free polymer. The chamber is sealed by an O-ring at the base, and there is a 9-pin vacuum feed through electrical connector for measurement signal readout. There are four holes at the top of the chamber. One is sealed. The other three are used for input and output of Hg vapor, and to purge the chamber.

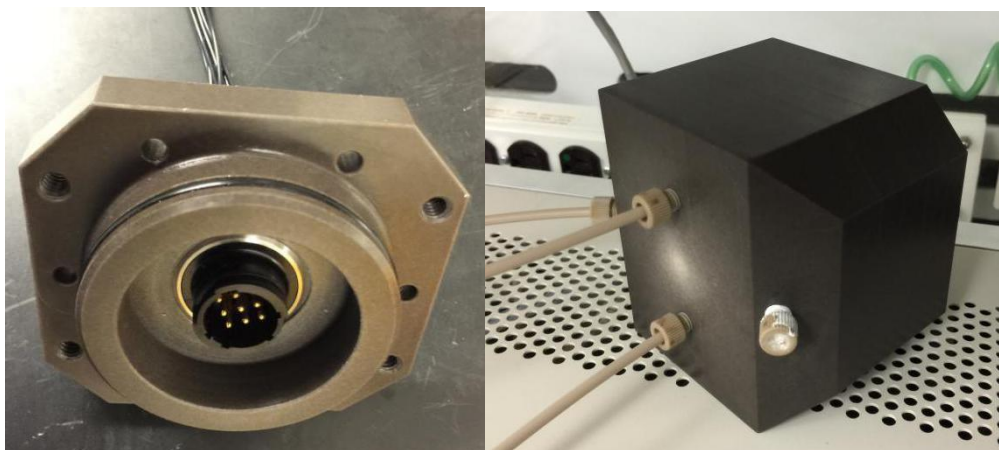


Figure 50 Structure of the test chamber

The airflow of the whole test setup is shown in Figure 51. Switch 1 and 2 are 3-way valves and valve 1 to 3 are two-way valves. Switch 1 can control airflow to purge the large outer container or go into the mercury generator. Switch 2 controls airflow to go through the mercury generator, carry mercury vapor into the test chamber or purge the test chamber.

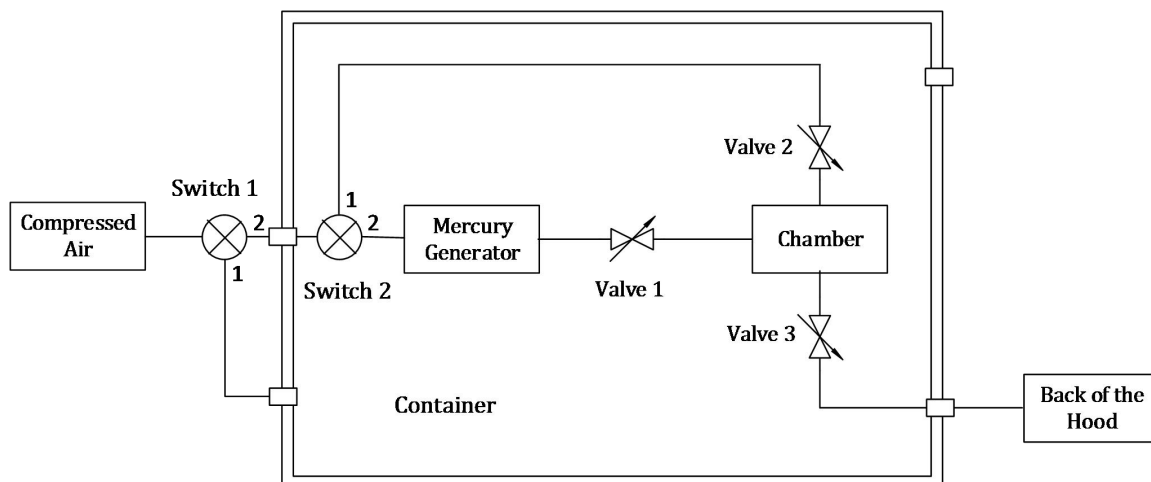


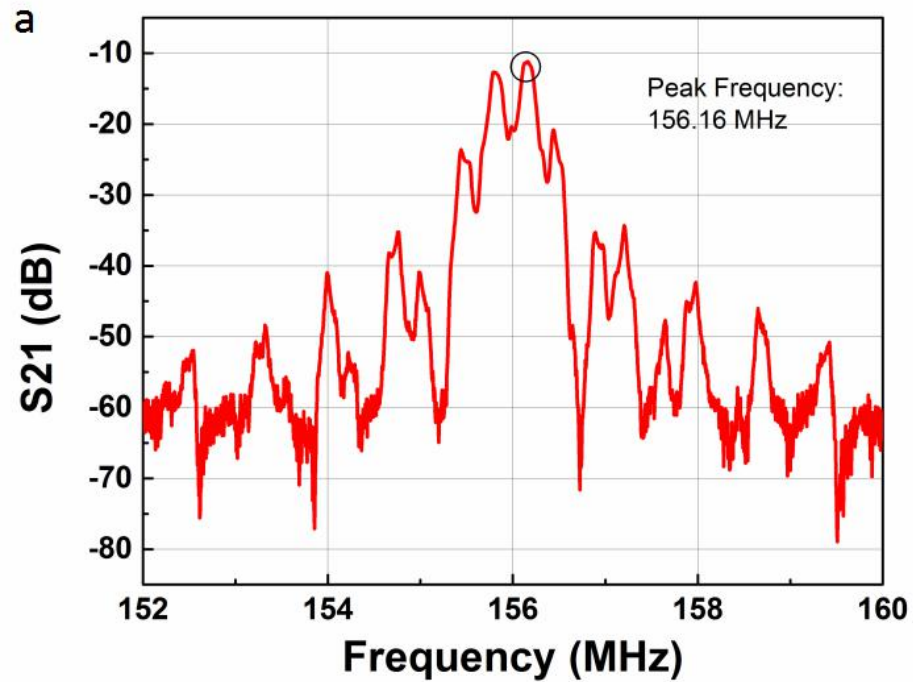
Figure 51 The schematic of test setup airflow.

A general description of a testing procedure is described as follows. When test starts, first purge the testing chamber. Then turn off the compressed air, open the test chamber to set the sensor. After the sensor is set, turn on the mercury generator to expose sample sensor to mercury vapor. After the test, turn off the mercury generator. Both the test chamber and the outer container should be purged.

4.2.2 Resonance frequency test

As mentioned in the previous section, 3 designs of SAW sensor with 20 μm pitch 5 μm electrode width, 20 μm pitch 6 μm electrode width and 24 μm pitch 7 μm electrode width were fabricated. The sensors were first tested with an Agilent Technologies N5230A Network Analyzer to get the resonance frequency. The frequency response of the SAW sensors with 20 μm pitch 5 μm electrode width, 20 μm pitch 6 μm electrode width and 24 μm pitch 7 μm electrode width are shown in Figure 52 (a), (b) and (c),

respectively. It can be observed from the test data that the maximum S21 values of two sensors with 20 μm pitch occur at 156.16 MHz and 155.69 MHz, respectively. Compare to the theoretical resonance frequency 157.9 MHz calculated by Equation (3), and the errors are within 2%. And the maximum S21 value of sensor with 24 μm pitch occurs at 130.3 MHz, compare to the theoretical resonance frequency 131.6 MHz calculated by Equation (3), the error is 0.9%.



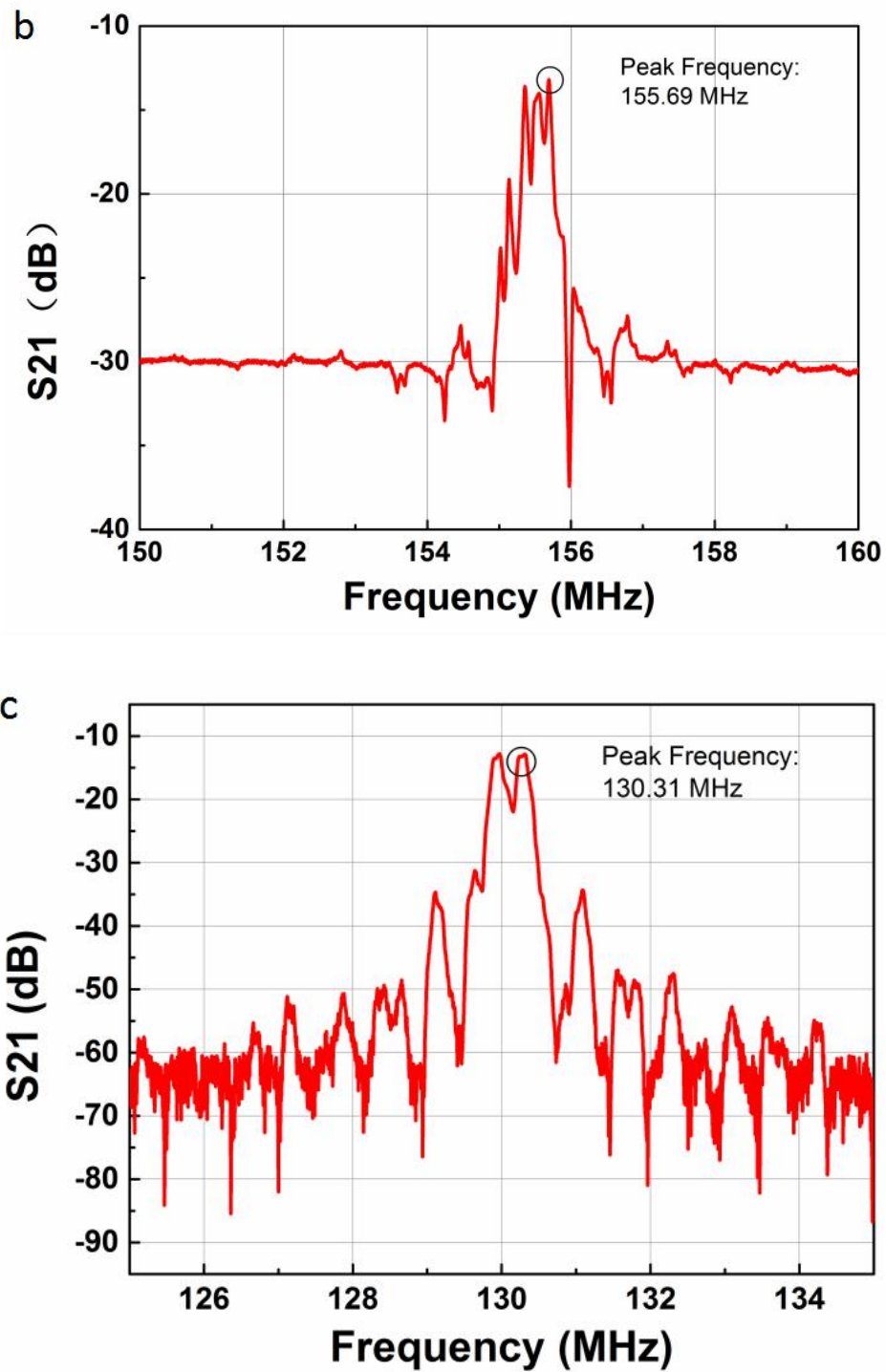


Figure 52 Measured frequency response of fabricated SAW sensor (a)20 μm pitch, 5 μm electrode width (b)20 μm pitch, 6 μm electrode width(c)24 μm pitch, 7 μm electrode width

The resonance frequencies of the fabricated SAW sensors are consistent with theoretical design. However the frequency response curves show the peaks are not clear but jagged. This will be discussed in the following sections.

4.2.3 Mercury vapor test

Then the sensors were tested with mercury vapor in the setup shown in Figure 51. For safety reason, the sensor was kept inside the clean room of LMST and analyzed with an HP 3589A network analyzer. Limited by the 10 Hz-150 MHz frequency range of the analyzer only the sensor with 24 μm pitch and 7 μm electrode width was tested.

The sensor was exposed to mercury vapor in the test chamber for 4 hours with 150 ng/m^3 mercury vapor at the flow rate of 0.52 L/min. To increase the contact of mercury vapor and the SAW sensor, the sample was fixed in the test chamber with scotch tape as shown in Figure 53. The sensor was directly faced to the mercury vapor input tube to maximum the contact probability. The resonance frequency of the exposed sensor was obtained.

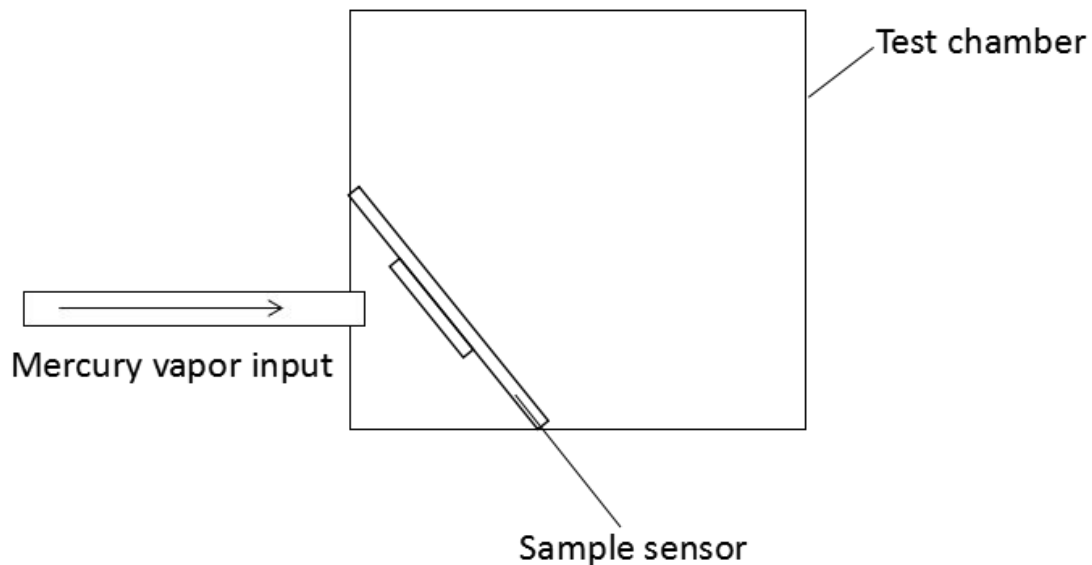


Figure 53 Schematic of sensor position in the test chamber.

The bond between mercury and gold will break when heated to certain temperature. Thus the regeneration process can be achieved. According to reference [54], around 1 hour heating on a 150°C hot plate can reach a full regeneration of mercury. Since the sample sensor didn't have direct contact with the hot plate, the efficiency of heat transfer would be lower. Consequently the sensor was heated on a 170°C hot plate for 1 hour. The frequency response of the sensor was obtained after cooling down.

CHAPTER FIVE: RESULTS AND DISCUSSION

5.1 Frequency Response Analyze

As shown in Figure 52, the resonance frequency of the fabricated sensors fit well with theoretical calculations; however the frequency response curves are jagged. This is caused by the internal reflection in the interdigital transducers[55]. The surface acoustic wave would be reflected by the IDTs when it propagates through the substrate surface. Though the single reflection is weak, when they were added into phase it could become powerful[55].

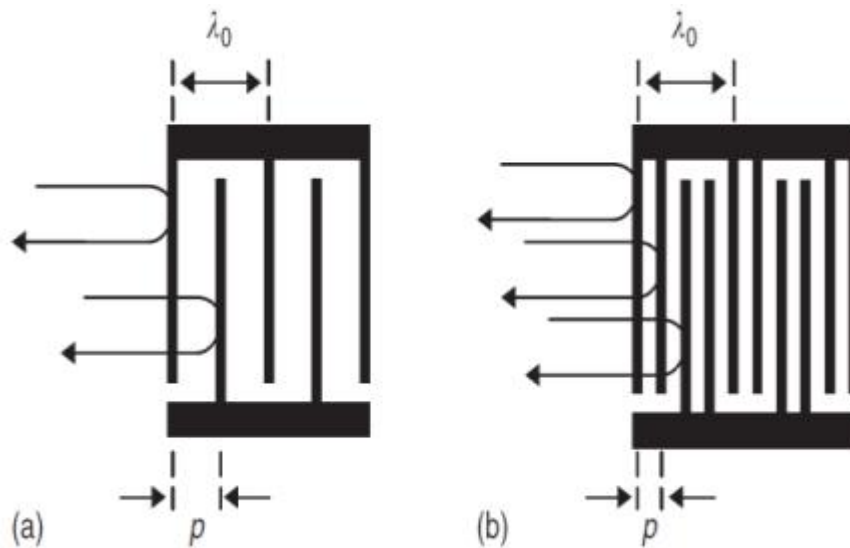


Figure 54 Internal reflection in (a) Single electrode IDT (b) Double electrode IDT[54]

The internal reflection can cause the deformation of IDT passband shape[56], that's the reason of the jagged resonance frequency curves. The performance can be improved by applying the double electrode IDT design[55].

The sensor also presented a fairly high noise level compared to the simulated result.

One of the major difference between the FEM model and sample sensor is that the substrate edge was not low-reflection boundaries. The surface acoustic wave can propagate much farther than other waveform without significant attenuation because it only travels along medium surface[34]. Since the length from IDT to the edge is on the same level of the delay line (2300 μm vs. 1400 μm), and no acoustic absorber was applied on the sample sensor, it is obviously the interference caused by reflected wave from the substrate edge cannot be eliminated. This is verified in the simulation model. A frequency domain simulation for the sensor with 24 μm pitch and 7 μm electrode width was carried out without low-reflection boundaries. Same frequency range and frequency steps as in the wide range frequency simulation were applied. Figure 55 (b) shows the result of this simulation. Compare to the previous result with low-reflection boundaries (Figure 55 (a)), clearly the noise level is much higher in the model without low-reflection boundaries. From this result it can be observed the interference of the wave reflected by the substrate edge is significant, an acoustic absorber is necessary for the improvement of sensor performance. The absorber can be added either during the fabrication process or manually after fabrication. Some commonly used material include waxes and epoxies, they are suitable for absorbing higher frequency waves[34]. Meanwhile, the silver epoxy adhesive used to connect the sensor with PCB plate might also be one of the reasons of high noise level.

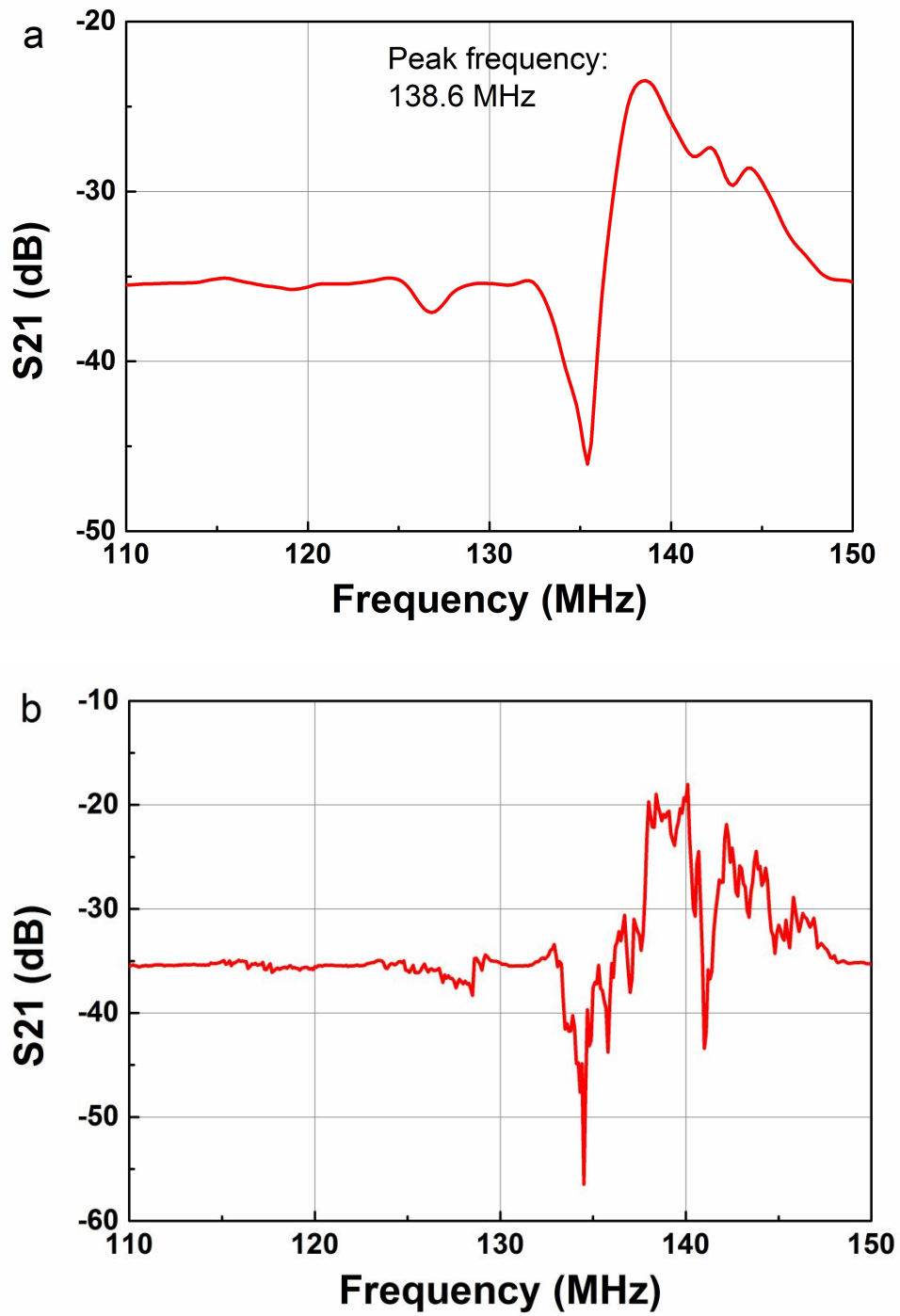


Figure 55 Simulated frequency response for sensor with 24 μm pitch and 7 μm electrode width (a)with low-reflection boundaries (b)without low-reflection boundaries.

5.2 Sensor Response To Mercury Vapor Exposure

The frequency response of the sensor exposed to mercury is shown in Figure 56. And the sensor frequency response after 1 hour heating is shown in Figure 57. The shape of response curve was consistent with the result in Figure 52. There are two peaks due to the shape of frequency response curve, the frequencies of both peaks were obtained. All data obtained is shown in Table 4. Both frequencies increased after heating. The reason could be after the exposure to the mercury vapor there was some mercury adsorbed on the gold electrode surface and caused the effect mass density increase of gold electrodes, which lead to a negative frequency shift. After the heating, the regeneration process happened so the mercury adsorbed by the gold electrodes was driven out, which made the mass density come back to normal. The resonance frequency returns to higher position with the density decrease. Due to the time issue this is the only mercury exposure experiment done. Though this result fits the theoretical model, no conclusion can be made through this result.

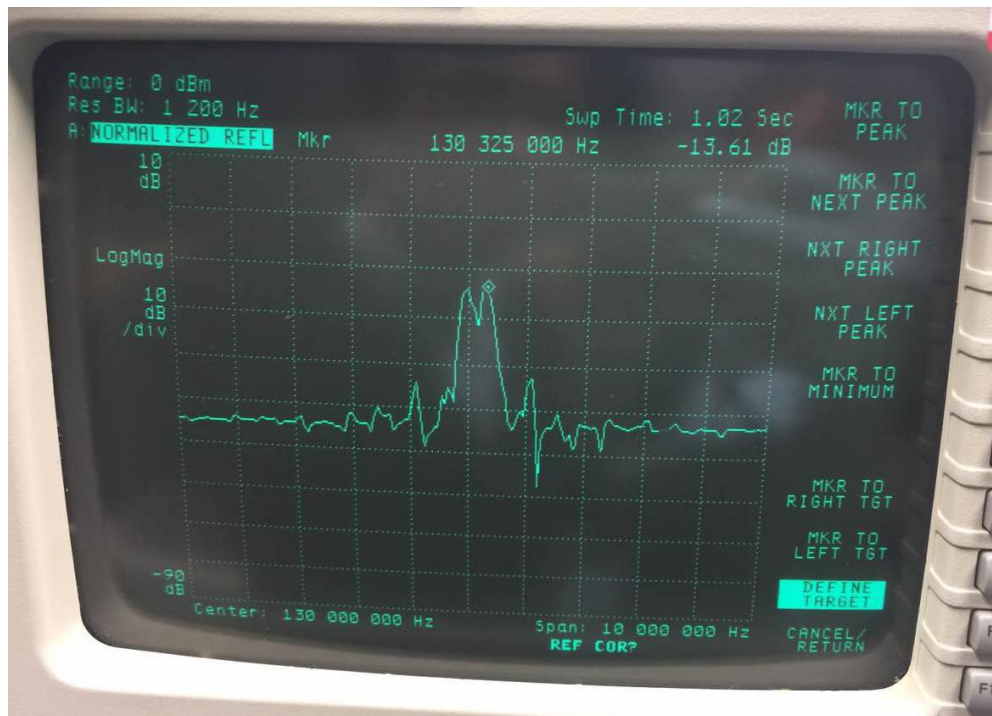


Figure 56 Sensor frequency response after exposed to mercury vapor.

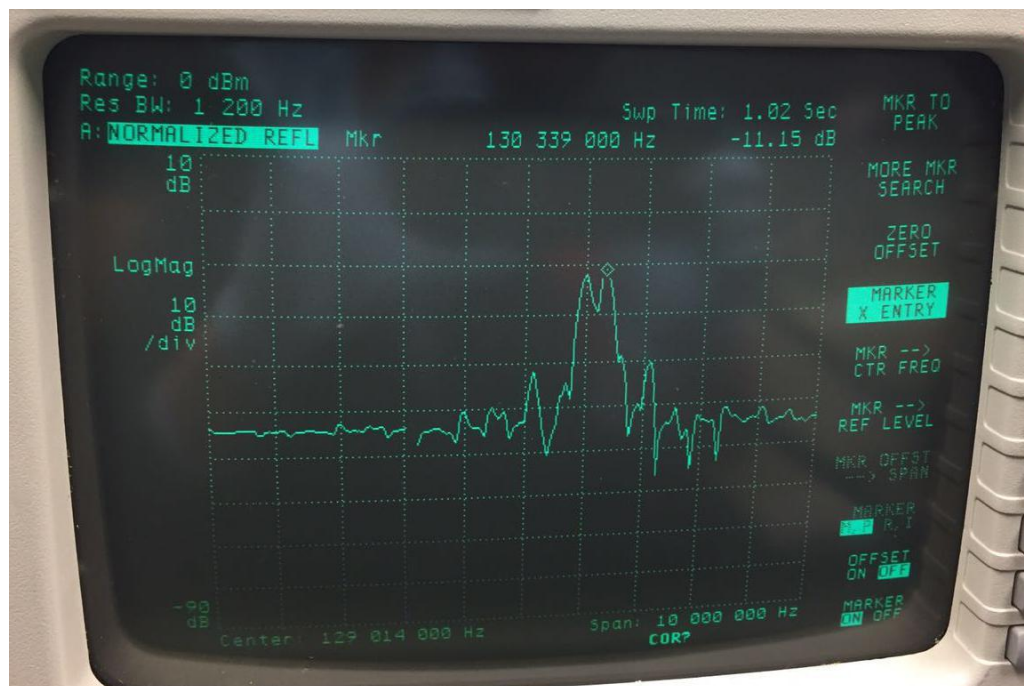


Figure 57 Sensor frequency response after heating.

Table 4 Frequency data from mercury exposure experiment.

	After mercury exposure	After heating	Δf
Left peak	129.975 MHz	129.989 MHz	+ 12 kHz
Right peak	130.325 MHz	130.339 MHz	+ 14 kHz

5.3 Summary

Through the experiments some good results were achieved. First of all, through the analyze of resonance frequency analyze the design and working principle of SAW sensor was verified. The fabricated sensor was proved capable of generating and transferring signals at certain frequency. The measured resonance frequencies of fabricated SAW sensors match the results from theoretical calculation and design. By this the fabrication technology was also proved to be valid. Though the response signal was interfered by the reflective wave, this still could be the foundation of following works. Second, a positive frequency shift was observed after heating the sample sensor exposed to mercury vapor. This result matches the theoretical model because after heating the bond between mercury and gold would break and the adsorbed mercury will be driven out[54], which leads to the effective mass density decrease of the gold electrodes. And the resonance frequency will have a positive shift due to the effective mass density change. Though

more experiments are needed to confirm this results, it shows the sensor could be sensitive to mercury vapor. Third, the shortcomings of the current sensor were analyzed and verified in simulation model. Through this improvements can be done based on results of this study.

There still are several inadequacies in the experiment. First, the sensor response before exposed to mercury was not obtained on the same network analyzer. Thus there was no reference to the resonance frequency obtained after mercury exposure. Even the result from heating regeneration process fits the theoretical model, the cycle of mercury adsorption - negative frequency shift - regeneration - resonance frequency return to original position was incomplete, the resonance frequency change observed in regeneration experiment cannot be confirmed to be attributed mercury adsorption. It could because the heating process drove out some other substance on the electrode such as moisture, which leads to the decrease of the effective mass density and consequently the increase of the resonance frequency.

Second, the connection between sample sensor and the network analyzer was very crude. The signal cable used on the analyzer did not match the SMA connectors welded on the sample sensor, and no adapter can be found due to the early production of the cable. The sensor was connected to the analyzer using copper wires and copper tapes. These are not suitable medium for high-frequency signals, this could cause errors in the

measurement.

Third, the repeatability of the experiment. Only one experiment was done because of the time limitation. It is unclear if the experiment can be repeated. And the frequency shift observed in the experiment was quite small compare to the magnitude of sensor resonance frequency. The frequency shift could be random error and cannot be confirmed without repeated experiment. The simulation results and experiment results were not directly compared since the simulation was based on the assumption of constant sticking coefficient and 100 % adsorption. This is far from the practical situation.

And no calibration was done before the mercury vapor test, the actual mercury vapor concentration was unconfirmed. This could bring error to the sensor characterization.

Last but not least, the results from FEM simulation for optimizing the sensor design were not verified. Limited by the time and the measuring range of the network analyzer, these experiments were not done. The design of sensor needs to be adjusted to the measurable range of network analyzer for these test.

CHAPTER SIX: CONCLUSION AND FUTURE WORK

6.1 Conclusion

This thesis aimed at designing and fabricating a surface acoustic wave sensor suitable for $1 \mu\text{g}/\text{m}^3$ level concentrated mercury vapor detection. Conventionally the delay line on SAW sensor is used as sensing element but a relatively novel design using the IDTs as sensing element was applied in this work. The working principle of SAW sensor was investigated, several prototype sensors were designed, fabricated and tested.

Specifically a FEM simulation model was built for the optimization of the sensor. Results from the FEM simulation showed that the sensor sensitivity could be improved by increasing the electrode width or decreasing the pitch of the sensor. The response time of the sensor was influenced both by the surface area and the sensitivity of the sensor. Based on these results an optimized sensor was designed. The testing results showed the working frequencies of fabricated SAW sensors fits well with the design and theoretical calculation. Limited by the time only one sensor was tested with mercury vapor exposure and heating regeneration. The results showed there was a positive frequency shift after heating which match the theoretical model but more experiments are needed to confirm the reason for frequency shift.

6.2 Potential Improvements And Future Work

There are some improvements can be done for the better performance of the sensor

and more future work is needed to verify the function of the sensor.

First, an acoustic absorber could be added to the sensor. With the absorber the interference of reflective wave can be eliminated and the sensor response can be more clear and stable. Second, a better way to connect the sensor to the network analyzer should be applied. The copper wire and copper tape used in this work is very crude and may cause significant errors, for a more accurate result a more stable way to connect the sensor and network analyzer is necessary. Also, the design of the sensor needs to be adjusted. Limited by the measurable frequency range of the network analyzer, only one of three fabricated sensor design was tested. The resonance frequency of the newly designed sensor has to be under 150 MHz. A better way to analyze the data should be found. Only by comparing the peak frequency cannot represent the change of sensor frequency response completely, the result would be more convincing if the shift of whole frequency response curve can be shown. And before the mercury vapor test a calibration could be done with some commercialized device.

Considering the results of this study, the potential future work could include: First, repeat experiment with the same sensor. At least 3 to 5 repeat experiments are needed to confirm the frequency shift observed in this work was not attributed to error in the measurement or the device. If the frequency shift can be repeated in the following experiments it can be concluded to be caused by the exposure process to mercury vapor

but still cannot be confirmed as mercury adsorption.

Second, the sensor can be tested in the same flow rate of air stream for the same amount of time. As mentioned before the working mechanism of the mercury generator used in this study is diluting the known concentration mercury vapor with air stream to desired concentration. It was observed during the experiments that blow moisture onto the sensor would influence the response, thus there could be interference contained in the air stream that caused the frequency shift of the SAW sensor.

If the reason for frequency shift can be attributed to mercury adsorption, sensor with different design can be tested to verify the influence of physical parameters on the sensor characteristics found in the simulation. Through these works a SAW sensor suitable for 1 $\mu\text{g}/\text{m}^3$ level concentrated mercury vapor detection can be made.

REFERENCES

- [1] "Mercury and the environment — Basic facts". Environment Canada, Federal Government of Canada. 2004. Retrieved 27 March 2008.
- [2] "Mercury — Element of the ancients". Center for Environmental Health Sciences, Dartmouth College. Retrieved 9 April 2012.
- [3] US-EPA, Mercury Study Report to Congress, Volume I, United States Environmental Protection Agency, 1997.
- [4] US-EPA, Mercury Study Report to Congress, Volume II, United States Environmental Protection Agency, 1997.
- [5] US-EPA, Mercury Study Report to Congress, Volume V, United States Environmental Protection Agency, 1997.
- [6] D.R. Nelson, Mercury attack of brazed aluminum heat exchangers in cryogenic gas service, Proceedings 73rd Annual GPA Convention, Gas Processors Association, 1994. 6
- [7] R.N. Bell, Understanding and Preventing Failure of Aluminum Equipment in the Presence of Liquid Mercury, Proceedings - American Institute of Chemical Engineers Spring Meeting, Atlanta, Georgia, 2005.
- [8] S. Mark Wilhelm, Risk Analysis for Operation of Aluminum Heat Exchangers Contaminated by Mercury, Process Safety Progress, September 2009, 28(3).
- [9] Jacob Dweck, Sonia Boutillon. Deadly LNG Incident Holds Key Lessons For Developers, Regulators. Pipeline & Gas Journal, May 2004, 231(5):39.
- [10] Harfoushian, J. H. (2013, September 30). Quantification of Low Levels of Mercury in Gas Reservoirs Using Advanced Sampling and Analysis Techniques. Society of Petroleum Engineers.
- [11] R.F. Fawer et al., Measurement of hand tremor induced by industrial exposure to metallic mercury. British Journal of Industrial Medicine, 1983, 40:204-208.
- [12] Leena Piikivi, u Tolonen, EEG findings in chlor-alkali workers subjected to low long term exposure to mercury vapour. British Journal of Industrial Medicine 1989, 46:370-375.

- [13] Leena Piikivi, Helena Hänninen, Finnish Institute of Occupational Health Danish National Research Centre for the Working Environment Norwegian National Institute of Occupational Health. *Scandinavian Journal of Work, Environment & Health*, Feb. 1989, 15(1):69-74.
- [14] G.D. Langolf, D. B. Chaffin, R. Henderson, and H. P. Whittle, Evaluation of workers exposed to elemental mercury using quantitative tests of tremor and neuromuscular functions, *American Industrial Hygiene Association Journal*, 1978, 39(2).
- [15] Forzi, M., et al. "Psychological measures in workers occupationally exposed to mercury vapours: A validation study." *Adverse Effects on Environmental Chemicals and Psychotropic Drugs: Neurophysiological and Behaviour Tests*, 1978, 2:165-171.
- [16] G. Kazantzis, K. F. R. Schiller, A. W. Asscher, R. G. Drew. Albuminuria And The Nephrotic Syndrome Following Exposure To Mercury And Its Compounds, *QJM: Quarterly Journal of Medicine*, Oct 1962, 31(4):403-418;
- [17] Raymond R. Tubbs, Gordon N. Gephardt, James T. McMahon, Marc C. Pohl, Donald G. Vidt, Sumner A. Barenberg, Rafael Valenzuela. Membranous Glomerulonephritis Associated with Industrial Mercury Exposure: Study of Pathogenetic Mechanisms. *American Journal of Clinical Pathology* Apr 1982, 77(4):409-413.
- [18] Jaffe KM, Shurtleff DB, Robertson WO. Survival After Acute Mercury Vapor Poisoning: Role of Intensive Supportive Care. *American Journal of Diseases of Children*, 1983;137(8):749-751.
- [19] C. Taueg, D. J. Sanfilippo, B. Rowens, J. Szejda, and J. L. Hesse. Acute and Chronic Poisoning from Residential Exposures to Elemental Mercury - Michigan, 1989–1990. *Journal Of Toxicology: Clinical Toxicology* 1992, 30(1).
- [20] Susana Río Segade, Julian F. Tyson. Determination of methylmercury and inorganic mercury in water samples by slurry sampling cold vapor atomic absorption spectrometry in a flow injection system after preconcentration on silica C18 modified. *Talanta*, March 2007, 71(4):1696–1702
- [21] The Royal Society of Chemistry Fine Chemicals and Medicinals Group. Atomic absorption spectrometry.

- [22] Daniel Martín-Yerga, María Begoña González-García, Agustín Costa-García. Electrochemical determination of mercury: A review. *Talanta*, 2013, 116:1091–1104.
- [23] Akul Mehta. Animation for the Principle of Fluorescence and UV-Visible Absorbance. *Analytical Chemistry, Animations, Notes*, March 20, 2013
- [24] F. James Holler, Douglas A. Skoog & Stanley R. Principles Of Instrumental Analysis. Crouch 2006.
- [25] http://www.uwm.edu.pl/kchem/mercury/afs_method.html
- [26] David Pfeil. Measurement Techniques for Mercury: Which Approach is Right for You? *IET* September / October 2011.
- [27] Micro- and nanomechanical sensors for environmental, chemical, and biological detection, Philip S. Waggoner, *Lab on a Chip*, 2007, 7:1238-1255
- [28] Paul D. Selid, Hanying Xu, E. Michael Collins, Marla Striped Face-Collins and Julia Xiaojun Zhao. Sensing Mercury for Biomedical and Environmental Monitoring. *Sensors* 2009, 9:5446-5459.
- [29] T. Thundat, E. A. Wachter, S. L. Sharp, and R. J. Warmack. Detection of mercury vapor using resonating microcantilevers. *Applied Physics Letters*, March 1995, 66(13).
- [30] Jir Homola, Sinclair S. Yee, Gunter Gauglitz. Surface plasmon resonance sensors: review. *Sensors and Actuators B* 1999, 54:3–15.
- [31] Jay Z. James, Donald Lucas and Catherine P. Koshland. Gold Nanoparticle Films As Sensitive and Reusable Elemental Mercury Sensors. *Environmental Science and Technology*, 2012, 46:9557–9562.
- [32] Milija Sarajlic, Zoran Đuric, Vesna Jovic, Srdan Petrovic, Dragana Đordevic. Detection limit for an adsorption-based mercury sensor. *Microelectronic Engineering*, 2013, 103:118–122
- [33] Joshua J. Caron, Reichl B. Haskell, Patrick Benoit, and John F. Vetelino. A Surface Acoustic Wave Mercury Vapor Sensor. *IEEE Transactions on Ultrasonics, Ferroelectrics, and Frequency Control*, Sept. 1998, 45(5).
- [34] Jared Kirschner, *Surface Acoustic Wave Sensors (SAWS): Design for Application, Microelectromechanical Systems*. December 6, 2010.

<http://www.jaredkirschner.com/uploads/9/6/1/0/9610588/saws.pdf>

- [35] K. M. Mohibul Kabir,^a Ylias M. Sabri,^a Glenn I. Matthews,^b Lathe A. Jones,^a Samuel J. Ippolito and Suresh K. Bhargava, Selective detection of elemental mercury vapor using a surface acoustic wave (SAW) sensor. *Analyst*, 2015, 140:5508
- [36] Vladimir M Mirsky, Majlinda Vasjari, Ivan Novotny, Vlastimil Rehacek, Vladimir Tvarozek and Otto S Wolfbeis, Self-assembled monolayers as selective filters for chemical sensors, *Nanotechnology*, 2002, 13:175–178
- [37] D. Ballantine Jr., R. M. White, S. J. Martin, A. J. Ricco, E. Zellers, G. Frye and H. Wohltjen, *Acoustic Wave Sensors: Theory, Design, and Physico-Chemical Applications*, Academic Press, 1996.
- [38] Madou, Marc J. “Scaling, Actuators, and Power in Miniaturized Systems.” *Fundamentals of Microfabrication: the Science of Miniaturization*. Boca Raton: CRC, 2002. 552-59
- [39] M. Levlin, E. Ikävalko, T. Laitinen. Adsorption of mercury on gold and silver surfaces. *Fresenius' Journal of Analytical Chemistry*, 1999, 365:577–586
- [40] E.S. Hirschorn, D.S. Lin, E.D. Hansen, T.-C. Chiang. Atomic burrowing and hole formation for Au growth on Ag(110). *Surface Science*, 1995, 323:L299-L304
- [41] Hank Wohltjen. Mechanism of Operation and Design Considerations for Surface Acoustic Wave Device Vapor Sensors. *Sensors & Actuators*, 1984, 5:307-325.
- [42] Auld, B.A. *Acoustic Fields and Waves in Solids*, Vol. II; Wiley Interscience: New York, 1973.
- [43] A.J. Ricco, S.J. Martin, T.E. Zipperian, Surface acoustic wave gas sensor based on film conductivity changes. *Sensors & Actuators*, 1985, 8(4).
- [44] M. Fialkowski, P. Grzeszczak, R. Nowakowski and R. Holyst, *Journal of Physical Chemistry*, B. 2004, 108:5026–5030.
- [45] Boston Piezo Optics Inc., Surface acoustic wave substrates.
- [46] Chin, Matthew L. “A Fabrication Study of a Surface Acoustic Wave Device for Magnetic Field Detection.” Thesis. Oregon State University, 2006. Scholars Archive at OSU. 5 June 2006. Web. 5 Dec. 2010.

- [47] T. Morris, J. Sun and G. Szulczewski. Measurement of the chemical and morphological changes that occur on gold surfaces following thermal desorption and acid dissolution of adsorbed mercury. *Analytica Chimica Acta*, 2003, 496: 279–287.
- [48] James JZ, Lucas D, Koshland CP. Gold nanoparticle films as sensitive and reusable elemental mercury sensors. *Environmental Science & Technology*. 2012, 46(17).
- [49] Lueke, J. A Mems-Based Fixed-Fixed Folded Spring Piezoelectric Energy Harvester. Ph.D. Thesis, University of Alberta, Edmonton, AB, Canada, 2014.
- [50] Jonathan Lueke, Ahmed Badr, Edmond Lou and Walied A. Moussa. Microfabrication and Integration of a Sol-Gel PZT Folded Spring Energy Harvester. *Sensors* 2015, 15:12218-12241.
- [51] AZ 5214E Product Data Sheet
- [52] Ho, C. Y., Powell, R. W., and Liley, P. E., *Journal of Physical Chemistry Ref. Data*, 1974 3:Suppl. 1.
- [53] Engineering Research Bulletin No. 40, Rutgers University (1958) quoted by Weast, R.C., Editor-in-Chief, *Handbook of Chemistry and Physics*, 48th edition, Cleveland: The Chemical Rubber Publishing Co. 1967-1968, page E-5.
- [54] Kwan Schambach, Klaus Eden, Klaus Schumacher, Gerhard Wiegleb. Micromachined Mercury Sensor. ESSDERC 2002
- [55] Sapna Tyagi and Varde G. Mahesh. Saw And Interdigital Transducers. *International Journal of Scientific & Engineering Research*, Dec. 2012, 3(12).
- [56] Ken-ya Hashimoto, Tatsuya Omori and Masatsune Yamaguchi. Design Considerations on Surface Acoustic Wave Resonators with Significant Internal Reflection in Interdigital Transducers. *IEEE Transactions on Ultrasonics, Ferroelectrics, and Frequency Control*, Nov. 2004, 51(11).

CURRICULUM VITAE

YISHEN LU

Personal information:

Year of Birth: 1993
 Phone: 617-852-5768
 Email: yishenlu@bu.edu

Address:

179 Babcock Street
 Apt 2
 Brookline, MA, 02446

EDUCATION

Boston University, College of Engineering, Boston, MA
 M.S. In Mechanical Engineering, January 2017

China University of Mining and Technology (CUMT), Xuzhou, China
 B.E. In Mechanical Engineering, June 2015

RESEARCH AND WORK EXPERIENCE

Laboratory for Microsystem Technology, Boston University, Boston, MA
 September 2016 - December 2016

Research Assistant

Designed, fabricated and tested a surface acoustic wave mercury vapor sensor.

Laboratory for Microsystem Technology, Boston University, Boston, MA
 January 2016 - July 2016

Lab Assistant

Studied the working principle of surface acoustic wave sensor, optimized the sensor design through FEM simulation.

Department of Mechanical Engineering, Boston University, Boston, MA
 September 2016 - December 2016

Grader for Mechanics of Materials (ME305), Fall 2016.

HONORS

Excellent Student of School of Mechanical Engineering, University Second class Rank scholarship, CUMT

Excellent Student Leader of China University of Mining and Technology, University First Rank scholarship

Learning Excellence Award of School of Mechanical Engineering, Third class scholarship

Second Prize in "Saint-Gobain Company" English Speech Contest held by School of Mechanical Engineering.

TECHNICAL SKILLS

CAD Modeling - AutoCAD, Solidworks

Finite Element Method Simulation - COMSOL Multiphysics, Mathematica

Data Analyze - Matlab, Originlab, MS Excel